The Relative Behavior of Shear Velocity, Bulk Sound Speed, and Compressional Velocity in the Mantle: Implications for Chemical and Thermal Structure

Guy Masters and Gabi Laske

IGPP, Scripps Institution of Oceanography, University of California, San Diego, La Jolla, California

Harold Bolton

Albuquerque Seismological Laboratory, Albuquerque, New Mexico

Adam Dziewonski

Dept. of Earth and Planetary Sciences, Harvard University, Cambridge, Massachusetts

Despite immense progress in imaging seismic velocity anomalies in the mantle over the past 15 years, we still know relatively little about their physical cause. One way to shed some light on this problem is to investigate the *relative* amplitudes of compressional and shear velocity anomalies in the mantle. Unfortunately, the amplitudes of velocity anomalies can be quite sensitive to the data sets and imaging techniques employed. It is therefore usually meaningless to take two models from the literature and do a simple comparison. In this paper, we consider joint modeling of P and S data sets and compare with some recent results from the literature. Some robust patterns are beginning to emerge which allow us to identify regions of the lower mantle which are anomalous. Such regions seem to be associated with large-scale upwelling in the mantle and may indicate chemical interaction with the core.

1. INTRODUCTION

During the past 15 years, our view of the seismic structure of the interior of the Earth has improved immensely. There is now general consensus on the gross 3D structure of the mantle: the upper mantle and lowermost mantle are characterized by large amplitude, long-wavelength structure while the mid-mantle contains low-amplitude slab-like fast features which surround broad regions of slow velocities.

Of course, we wish to go beyond the stage of merely mapping the mantle and proceed to the next step of interpreting the maps in terms of the thermal and chemical structure. One way of doing this is to investigate the *relative* behavior of the compressional and shear velocities in the mantle since we have a reasonable understanding of how this should vary for purely (sub-solidus) thermal effects from laboratory experiments.

To do this, we need to have good estimates of the *size* of velocity anomalies in the mantle as well as their shape. The size of anomalies can often be quite poorly determined

Earth's Deep Interior: Mineral Physics and Tomography From the Atomic to the Global Scale
Geophysical Monograph 117

Table 1. High temperature experimental values from Anderson and Isaak (1995). Θ is the Debye temperature.

Substance	R	ζ	T/Θ
NaCl	1.2	1.3	2.0
KCl	1.2	1.3	2.0
MgO	1.2	1.6	1.5
CaO	1.2	1.5	1.5
MnO	1.6	2.4	1.0
Al_2O_3	1.4	2.2	1.5
Mn_2SiO_4	1.2	1.3	1.3
Co_2SiO_4	1.0	0.9	1.3
Fe_2SiO_4	0.9	0.9	1.2
Mg_2SiO_4	1.2	1.4	2.0
Olivine	1.2	1.4	2.0
Pyrope	1.1	1.0	1.3
Grossular	1.3	1.8	1.5
$Mg_2Al_2O_4$	0.9	0.8	1.1

and can depend on the data sets used as well as details of the inversion procedure. Usually, data sets have very uneven sampling characteristics, and to take advantage of the densest sampling, tomographic models are often grossly overparameterised. This can lead to instability in the inversion and to strong dependence on regularizing criteria. A common consequence is that amplitudes are underestimated. Often, the relative sampling of S and P data sets can be quite different so the degree of smoothing for each velocity type is different resulting in spurious values for their relative behavior.

We believe that one promising approach is to use many different data types such as mode structure coefficients, surface wave dispersion, and absolute and differential travel times, jointly in the inversions. To give a feel for what can be reliably determined from such data, we spend a significant fraction of this paper discussing different data types and the patterns of heterogeneity that they reveal. We also compare long- and short-period body wave data sets to convince ourselves that these data do not "see" fundamentally different Earths.

We follow this with a discussion of high-resolution modeling where we find that such inversions are relatively stable with no strong dependence on inversion technique provided the systems to be solved are reasonably well-conditioned. Some experiments in joint modeling follow where we concentrate on joint inversions of shear velocity and bulk sound speed. When we compare our results with those from the literature, we find good agreement with an inversion which uses multiple data types in a similar fashion to our experiments but poor agreement with inversions based primarily on ISC travel time data. We speculate on reasons for the disagreements and give arguments in favor of those models with larger velocity anomalies in the mid mantle and transition zone. We conclude with some preliminary results about the relative behavior of shear and compressional velocity in the mantle and speculate about their cause.

2. THERMODYNAMIC BACKGROUND

We shall be considering three seismic velocities: the compressional velocity, v_p, the shear velocity, v_s, and the bulk sound speed, v_c. These velocities are related to the bulk modulus, K_s, the rigidity, μ, and the density, ρ, by

$$K_s = \rho v_c^2 = \rho(v_p^2 - \frac{4}{3}v_s^2); \qquad \mu = \rho v_s^2 \tag{1}$$

It therefore follows that

$$\frac{\delta v_p}{v_p} = \gamma\frac{\delta v_s}{v_s} + (1-\gamma)\frac{\delta v_c}{v_c}; \qquad \gamma = \frac{4}{3}\frac{v_s^2}{v_p^2} \tag{2}$$

where $\gamma = 0.40 \pm 0.02$ for plausible models of the mantle. Clearly, the variation in compressional velocity is almost as sensitive to variation in shear velocity (rigidity) as to variation in bulk sound speed (bulk modulus). Several studies have used the relative variation in shear and compressional velocity as a diagnostic of the physical cause of an anomaly but it may be better to use the relative variation of shear velocity to bulk sound speed. We therefore define:

$$R = \frac{\partial \ln v_s}{\partial \ln v_p}; \qquad \zeta = \frac{\partial \ln v_s}{\partial \ln v_c} \tag{3}$$

These are easily shown to be related by

$$R = \frac{\zeta}{\zeta\gamma + 1 - \gamma}; \qquad \zeta = \frac{(1-\gamma)R}{1-\gamma R} \tag{4}$$

An advantage of using the logarithmic ratio, R, is that its value, as determined by laboratory experiments, varies little from material to material. *Anderson and Isaak* [1995] summarize the high temperature experimental results for a wide variety of materials and find R between 0.9 and 1.6 (Table 1). This result has been the basis for using $R \approx 1.3$ in seismic studies where it is necessary to scale between shear and compressional velocities [*Masters et al.*, 1982; *Forte & Peltier*, 1987; *Woodward & Masters*, 1992; *Masters et al.*, 1996]. ζ has a mean value of about 1.5 but it varies from material to material more than R does. For this reason, we will focus on R in the following.

Karato [1993] has pointed out that the laboratory value for R may not be appropriate for application to the Earth since anelastic as well as anharmonic effects are important. In real materials, relaxation processes occur which affect the seismic velocity and make it dependent on frequency. Since relaxation processes are usually thermally activated, a change in temperature changes the characteristic frequency of the process and so changes the elastic velocities. For a frequency-

independent Q, the seismic velocity depends on frequency and temperature (T) as [*Kanamori and Anderson*, 1977]

$$v(\omega, T) = v_0(T)\left[1 + \frac{1}{\pi Q}\ln(\omega\tau)\right] \quad (5)$$

where v_0 is a reference velocity corresponding to the unrelaxed state and the relaxation time, τ, is a function of temperature of the form

$$\tau(T) = \tau_0 \exp(H^*/R_g T) \quad (6)$$

where H^* is the activation enthalpy and R_g is the gas constant. Differentiating equation (5) with respect to temperature gives

$$\frac{\partial \ln v}{\partial T} = \frac{\partial \ln v_0}{\partial T} - \frac{1}{\pi Q}\frac{H^*}{R_g T^2} \quad (7)$$

where attenuation has been assumed to be weak ($Q \gg 1$). The first term in equation (7) corresponds to the anharmonic effect while the second term represents anelastic effects. The importance of the latter will be greatest in zones of high attenuation where Q is low. The size of the effect is also strongly dependent on the activation enthalpy, H^*, which is poorly known in the lower mantle. Using data for olivine, *Karato* [1993] estimates that R (which is 1.2 in the infinite frequency limit) will increase to about 1.6 for a Q_μ of 100 and to 1.8 for a Q_μ of 50. He also estimates that this effect will be important throughout the mantle giving R values of the order of 1.7 (though the estimate is very uncertain).

Several of the seismic results described below suggest an R which is higher than that found in laboratory experiments and this fact has stimulated some theoretical work on the properties of lower mantle phases. *Agnon & Bukowinski* [1990] and *Isaak et al.* [1992] show that a value of $R \simeq 2 - 2.5$ for a possible lower mantle constituent (MgO) is consistent with a theoretically predicted, pressure-induced decrease in the Anderson-Grüneisen parameter $\delta_S = -(1/\alpha K_s)(\partial K_s/\partial T)_P$. (Here α is the coefficient of volume thermal expansivity, K_s is the adiabatic bulk modulus, and P is pressure.) A more recent analysis by *Karato et al.* [1999] again indicates higher values for R for purely thermal effects with a value of 1.8 at the top of the lower mantle rising to perhaps as much as 2.2 at the base of the mantle. Such values are still too low to cause bulk sound speed to be negatively correlated with shear velocity (equation 4) but this is a feature of several lower mantle models (see below).

In the next section, we consider some of the data sets that go into the construction of tomographic models. In particular, it is of interest to make rough estimates of R from the data using

$$R \approx \frac{v_s}{v_p}\frac{\delta t_s}{\delta t_p} \quad (8)$$

where δt_s and δt_p are perturbations to the spherically averaged body wave travel times. This relationship between R and the travel time perturbations is derived from Fermat's principle and assumes that the perturbations in both the P and S seismic velocities which cause the travel time anomalies are co-located [*Souriau & Woodhouse*, 1985].

3. DATA TYPES

3.1. Body Wave Travel Times

Historically, travel times have been measured from short-period vertical-component instruments on which P arrivals typically have a dominant period of 1 s and S arrivals have a dominant period of about 4 s. Many such instruments distributed around the world still record such data. The arrival times are measured locally and then compiled and distributed by the International Seismological Centre (ISC). These data are published in the Bulletins of the International Seismological Centre and subsets of this data set (typically the first-arriving P wave times which now number several million) have been used to refine existing 1-dimensional models [*Dziewonski & Anderson*, 1981; *Kennett & Engdahl*, 1991; *Morelli and Dziewonski*, 1993; *Kennett et al.*, 1995] and in tomographic studies of 3-dimensional structure [*Clayton & Comer*, 1983; *Dziewonski*, 1984; *Creager & Jordan*, 1986; *Morelli et al.*, 1986; *Morelli & Dziewonski*, 1987; *Shearer et al.*, 1988; *Inoue et al.*, 1990; *Pulliam*, 1991; *Pulliam et al.*, 1993; *Vasco et al.*, 1993, 1994, 1995; *Vasco and Johnson*, 1998; *Su et al.*, 1994; *Su and Dziewonski*, 1997; *Van der Hilst et al.*, 1997; *Zhou*, 1996; *Kennett et al.*, 1998; *Bijwaard et al.*, 1998].

The strength of the ISC data set is its size but the fact that it is composed of readings from many different instruments (of varying quality) made by many different operators means that it is a very noisy and inhomogeneous data set. *Gudmundsson et al.* [1990] estimate the signal to noise (S/N) ratio of the ISC P-data to be less than 1.0 at local and regional distances and approximately 2 for teleseismic P. A major reprocessing of the ISC data set has been undertaken by *Engdahl et al.* [1998] (hereafter EHB) with particular attention paid to the problem of misidentification of depth phases for direct phases. It is this reprocessed data set that has been used in the most recent tomographic modeling [*Van der Hilst et al.*, 1997; *Bijwaard et al.*, 1998; *Kennett et al.*, 1998].

ISC S wave times are typically very noisy because their low-frequency character is not well-recorded by short-period instruments and phase misidentification (particularly with SKS at distances beyond 80 degrees) is common since picking is typically done only from vertical component recordings. This makes it extremely difficult to use the ISC data set to do a comparative study of the lateral variations in P and S velocity though there have been a few recent efforts [*Robertson & Woodhouse*, 1995, 1996; *Kennett et al.*, 1998; *Vasco & Johnson*, 1998].

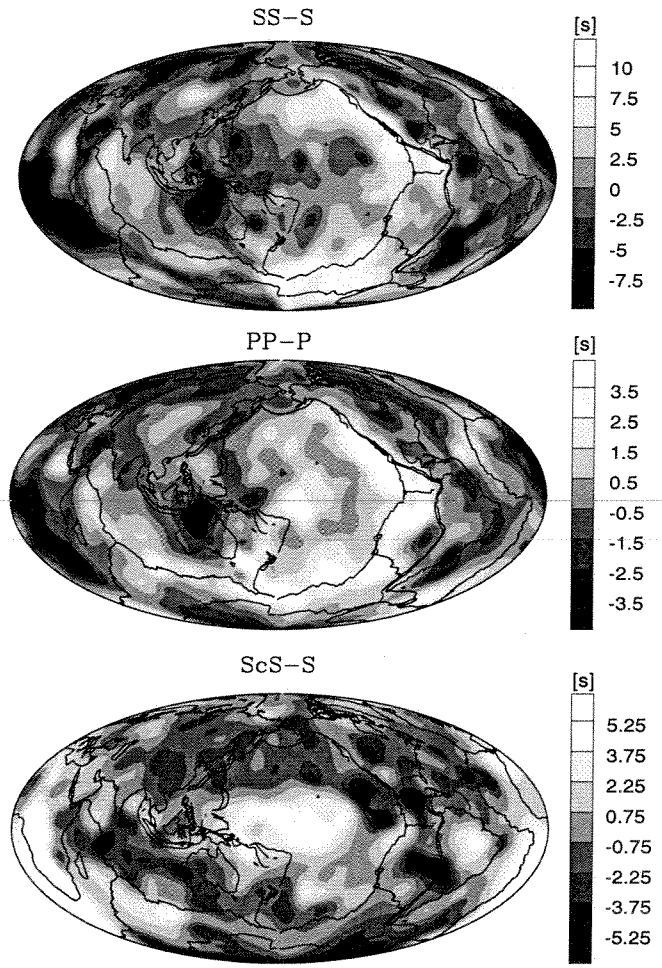

Figure 1. Travel time residual patterns for $SS - S$, $PP - P$, and $ScS - S$ differential times. These maps are made by lightly smoothing the pattern of residuals obtained by plotting the residual at the bouncepoint of SS, PP, and ScS respectively. The $SS - S$ and $PP - P$ maps are highly correlated (though there are significant differences) with an $SS - S$ residual being typically 3 times a $PP - P$ residual. Many of the features seen in the $SS - S$ and $PP - P$ maps are clearly related to near-surface tectonics while the $ScS - S$ map is quite different.

Since the mid 1970's, digital recordings of relatively long-period body waves (about 20 s dominant period) have become available and have been analyzed in many different ways. The waveforms can be directly modeled for aspherical structure using a variety of theoretical approximations [*Woodhouse & Dziewonski*, 1984; *Dziewonski & Woodhouse*, 1987; *Tanimoto*, 1990; *Li and Romanowicz*, 1995, 1996; *Su & Dziewonski*, 1991]. Alternatively, absolute and differential travel times can be estimated directly from the data and have been used in more traditional tomographic studies [*Woodward & Masters*, 1991a,b,1992; *Masters et al.*, 1996].

The fact that the long-period data have longer wavelengths than the waveforms used for the ISC data set has both advantages and drawbacks. An advantage is that it is possible to construct data sets with little spatial aliasing though, of course, resolving short-wavelength structure is much more difficult. Another advantage is that the long-period data show few of the effects of scattering so evident in short-period data. This makes it very easy to pick secondary phases since codas are practically nonexistent. Another advantage is that both P and S long-period waveforms have similar frequency content as this is now controlled by the instrument response rather than the attenuation characteristics of the Earth. This makes the effects of physical dispersion much easier to assess. Currently we have measured approximately 41,000 S and 38,000 P long-period travel times at teleseismic distance ranges [*Bolton & Masters*, 1999], 18,000 $SS - S$ differential times, 12,000 $PP - P$ times, and 8000 $ScS - S$ times. Fig. 1 illustrates the residual patterns for $SS - S$, $PP - P$, and $ScS - S$. These maps are made by lightly smoothing the pattern of residuals obtained by plotting the residual at the bouncepoint of SS, PP, and ScS respectively. The $SS - S$ and $PP - P$ maps are highly correlated (though there are significant differences) with an $SS - S$ residual being typically 3 times a $PP - P$ residual [*Woodward and Masters*, 1991a]. We take this as representative of upper mantle structure (leading to an R value of about 1.7). Many of the features seen in the $SS - S$ and $PP - P$ maps are clearly related to near-surface tectonics while the $ScS - S$ map is quite different. Here, we see slow areas under Africa and the central Pacific with a ring of fast residuals around the Pacific. Not surprisingly, these features are reproduced in the lowermost mantle of almost all recent tomographic models.

Crustal structure, particularly structure directly under the receiver can contribute quite strongly to the measured absolute times. One way to account for this effect is to apply "station corrections" (i.e., mean station residuals usually corrected for uneven azimuthal distribution) to the data. Such corrections have been calculated for the ISC data set by a number of authors [e.g., *Dziewonski and Anderson*, 1983; *Toy*, 1989]. Of course, such corrections remove more than just the signal of the crust, they also effectively remove the upper mantle and possibly some of the lower mantle as well. Since we are interested in structure throughout the mantle, we elect to not use station corrections but correct for the crust using the global crustal model, CRUST 5.1, of *Mooney et al.*, [1998]. It is, however, interesting to note that most studies of station corrections find a typical 3:1 ratio between the S and P station means in agreement with the $SS - S/PP - P$ value discussed above.

Fig. 2 shows histograms of the S and P residuals binned by ray turning depth. This figure shows the remarkable increase in variance for S residuals as one samples deeper in the mantle which is apparently absent in the P data. It is noteworthy that the ISC defines a teleseismic S as anything within 7.5 seconds of the Jeffreys-Bullen (JB) predicted times. It is

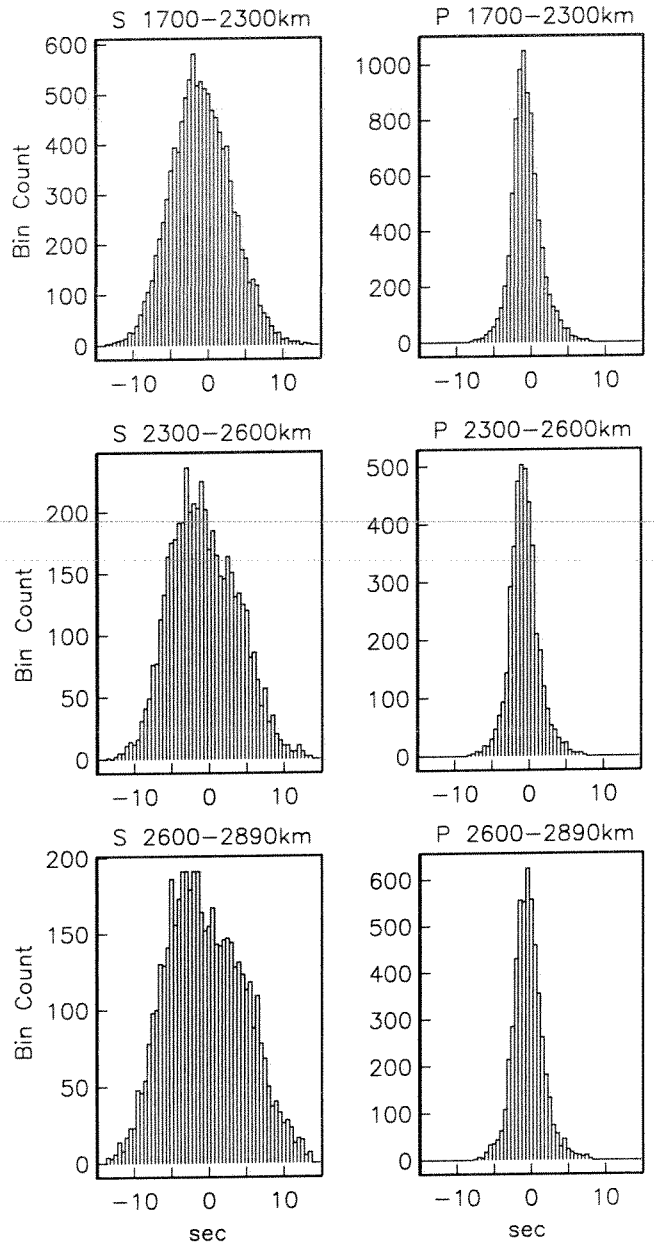

Figure 2. Histograms of the detrended P and S residuals as a function of ray turning depth. Note the significantly larger variance for S compared to P residuals. The variance of S residuals increases with depth where a good fraction of the data have a signal of more than 7.5 sec, the cut-off for S picks in the ISC catalog.

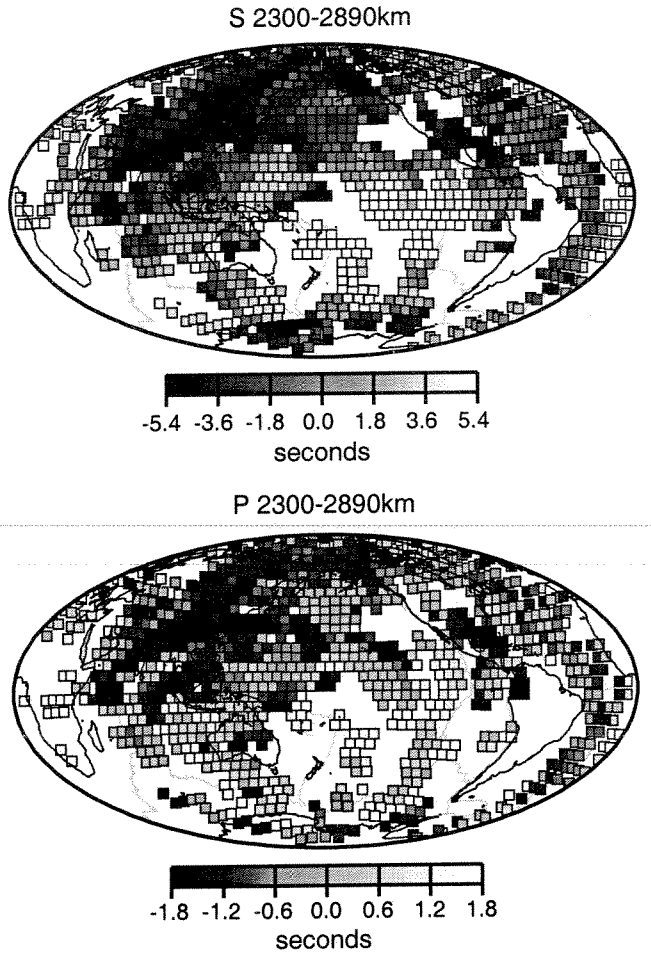

Figure 3. 5° spherical cap averages of our detrended S and P residuals plotted at their ray turning points for rays which bottom in the lower 600 km of the mantle. The regions of slow S residuals under the Pacific and Africa are clearly visible though these are more muted in the P map.

quite clear from Fig. 2 that long-period S residuals span a much larger range than this, and this is also true of short period S [*Robertson and Woodhouse*, 1995]. Consequently, any inversion which restricts attention to the ISC-defined S arrivals will underestimate the size of S anomalies in the mantle.

The increase in variance in S residuals with ray turning depth is mainly due to the appearance of very slow S residuals for rays which bottom under the central Pacific and under Africa. We illustrate this in Fig. 3 where we bin rays which have similar turning points and plot the resulting smoothed residuals at the turning point. The slow areas in the S map are much more pronounced than in the P map – this suggests that we may have to appeal to an effect such as partial melting to explain the relative behavior of P and S in these regions. If we plot co-located P and S mean residuals against each other for a variety of turning depth ranges, we obtain Fig. 4. Slopes are calculated by solving the "Least-Squares Cubic" [*York*, 1966] for the best fitting line. For the rays turning between 670-1100km we find a slope of about 3.3 ($R \sim 1.8$), in close agreement with that found for the long-period $SS-S/PP-P$ ratio. Between 1100-2000km the slope increases to about 4 ($R \sim 2.2$). We see a steady increase in the slope starting

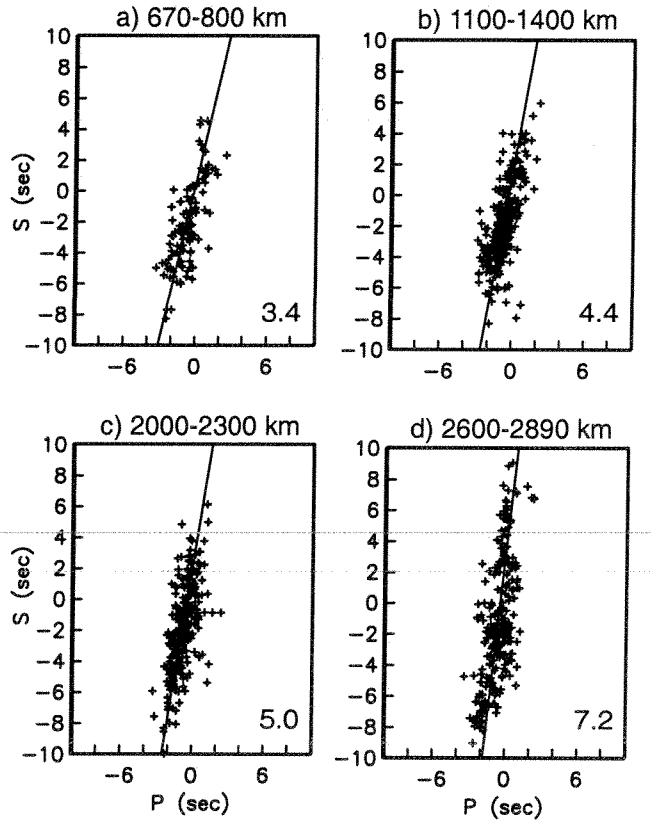

Figure 4. Scatter plots of S and P cap averages of residuals binned by turning depth (there are a minimum of 5 picks per cap). The ratio of the residuals (i.e., the slope) increases steadily with ray turning depth with a sharp increase for the deepest turning rays. The slopes for a-d are given in the lower right corner.

at about 2000km depth. For the deepest turning rays (2600-2890km), we see a further increase to a slope of about 7 ($R \sim 3.8$). Clearly, such high values of R are very different from what we expect for normal thermal effects.

3.2. *Comparing Long and Short Period Data*

In the following sections, we will find that there are quite large differences in the amplitudes of S and P anomalies in the mantle determined by different researchers. It is of interest to see if this is due to fundamental differences in the data sets employed, or if it is a product of data selection and/or modeling technique. To clarify the comparison, we restrict attention to stations which report short period data to the ISC and also record broad-band digital data from which our long-period picks have been made. We form "summary rays" by grouping residuals from clusters of earthquakes and then plot the median residual of the summary ray at its turning point. All residuals are computed using the EHB locations. Fig. 5 shows a comparison of the resulting smoothed residual patterns for station MAT/MAJO. This station is unusual in that it has a relatively large number of S picks (~4000) as well as P picks. The patterns in both S and P are very similar though the amplitude of the patterns in the short period data are a little smaller than in the long period data. It is interesting to explore the internal consistency of the data by looking at the variability within each summary ray. For summary rays with more than a few tens of measurements, we find that the ISC P data have a standard deviation of about 0.4–0.5 seconds while the long-period data are about twice this. The situation is reversed for S where the standard deviation of a group of rays constituting a summary ray is about 1.3 seconds for the long-period data and about twice this for the ISC data. Also, as noted above, there are few ISC S data beyond 80 degrees and these tend to be extremely noisy. MAT has a respectable number of S picks but other stations, e.g. NWA/NWAO, have only a few hundred S picks that are confined to a small azimuth range (Fig. 6). This suggests that studies which use ISC data and conservatively confine attention to only those paths that have common S and P will be restricted to using a relatively small portion of the data.

We conclude from this brief comparison that residual patterns in long and short period data are indeed similar and our analysis of errors suggests that the optimal approach may be to use ISC P data combined with long-period S data (as was done by *Su and Dziewonski*, [1997]).

3.3. *Surface Waves*

It is extremely difficult to constrain structure in the upper mantle and transition zone using body waves alone unless triplication phases of multiple surface bounce arrivals are included [*Grand*, 1994]. Such an analysis is delicate and time-consuming and a simpler way to constrain near-surface structure is to include surface waves.

Global surface wave phase velocity maps have been constructed by numerous workers by measuring surface wave dispersion [e.g. *Montagner & Tanimoto* 1990; *Laske and Masters*, 1996; *Ekström et al.*, 1997; *Trampert and Woodhouse*, 1995, 1996; *Zhang and Lay*, 1996] though some of these studies have also included polarization data to improve sensitivity to short wavelength structure. There is now good agreement between phase velocity maps for periods between 50 and 150 seconds up to relatively short wavelengths. An example is shown in Fig. 7.

Global phase velocity maps are typically dominated by large-amplitude long-wavelength structure (Fig. 8). Though the spectral amplitudes of such maps are somewhat uncertain, it is probably fair to say that the maps of *Trampert and Woodhouse* [1996] are slightly too rough and that the amplitudes of *Zhang and Lay* [1996] are too low, hence placing reasonable error bounds on spectral amplitudes. The correlation of such maps at spherical harmonic degrees $\ell = 10$ and lower is typically well above the 99% confidence limit though it appears that the inclusion of higher orbit and great-circle dispersion

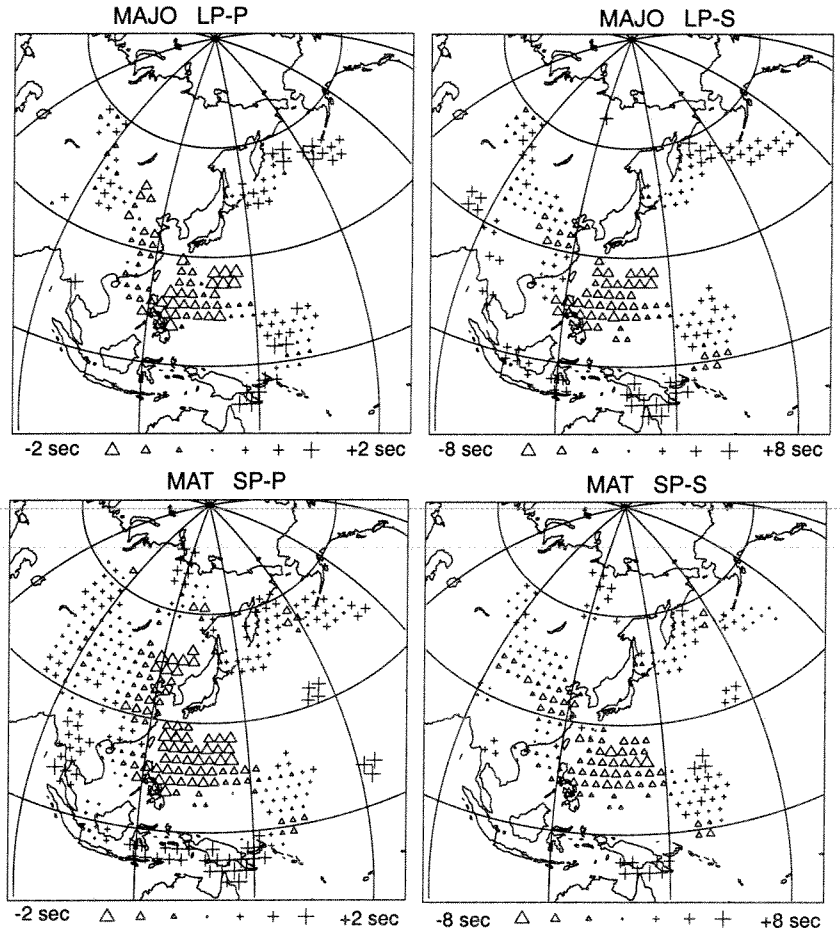

Figure 5. The medians of summary rays (see text) for the stations MAJO/MAT plotted at the surface projection of the summary ray turning points. MAJO is a broad band station, from which we have made long-period picks, co-located with MAT which is a short period station which reports to the ISC. There is extremely good correspondence between the long and short period picks though the coverage of the short period P is much better than for the long period data. There is also extremely good correlation between the patterns in P and S.

data is needed to obtain results compatible with the mode structure coefficients (see below and Fig. 9). At harmonic degrees higher than $\ell = 16$, the correlation between maps of different workers is significantly reduced with the best correlation being between the maps of *Ekström et al.* [1997] and *Trampert and Woodhouse* [1995]. Both of these groups use a large amount of mainly minor arc phase data to obtain sensitivity to short wavelength structure. *Laske and Masters* [1996] have much less data though they use polarization data that give independent sensitivity to short wavelengths. It should be pointed out that the reduction in correlation is also accompanied by a reduction in amplitude so many of the differences at short wavelength are barely significant.

Surface waves have some sensitivity to density as well as to elastic velocities. The proper procedure in a tomographic study would be to include density as an additional free parameter in the modeling. The limited amount of data allows numerous trade-offs between (anisotropic) elastic velocities and density (see next section for a specific inversion) so most of our modeling assumes that density can be scaled to shear velocity using the relationship $dlnv_s/dln\rho = 2.5$. The exact value has no impact on the inversion of Love waves (since these are virtually insensitive to density) but has a minor effect on the inversion of Rayleigh waves for structure in the top 250 km of the mantle.

3.4. Mode Structure Coefficients

Free oscillation structure coefficients [see e.g. *Ritzwoller et al.*, 1986, 1988; *Giardini et al.*, 1987,1988] provide constraints on the long-wavelength structure of the Earth with principal sensitivity to structure of even harmonic degree. This kind of data has been used previously to look at the relative variation of v_s to v_p [*Li et al.*, 1991] though the data sets available now are much more precise. In principle, these

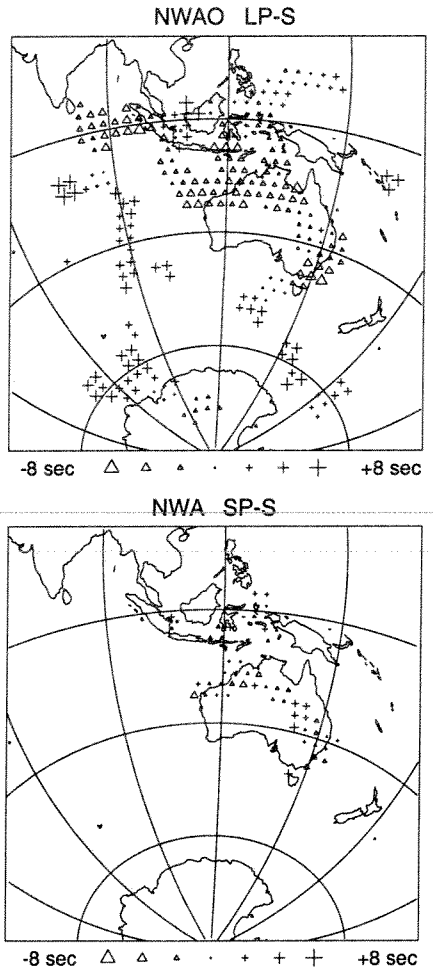

Figure 6. The medians of S summary rays for the stations NWAO/NWA plotted at the surface projection of the summary ray turning points. NWAO is a broad band station, from which we have made long-period picks, co-located with NWA which is a short period station which reports to the ISC. Note the small number of S picks for NWA and the small range of azimuth they cover.

data are also sensitive to 3D density variations as well as to 3D elasticity though we shall find that the current data set is still not precise enough to make any definitive conclusions about 3D density.

The analysis of free oscillations has seen something of a renaissance in the past few years because of the recent occurrence of several "great" earthquakes, including the great Bolivian earthquake of 1994 which was at a depth of 630km. We have combined data from several recent analyses [*He and Tromp*, 1996; *Resovsky and Ritzwoller*, 1998; *Um*, personal communication, 1996; *Masters et al.*, 1999] along with older peak-shift data [e.g. *Smith and Masters*, 1989] to give a new data set of structure coefficients of degrees 2,4 and 6 for 50 fundamental spheroidal mode, 26 spheroidal overtones, 31 fundamental toroidal modes, and 12 toroidal overtones. The structure coefficients of degree 2 are by far the best determined and also show the largest signal. Fig. 9 shows these coefficients for the fundamental spheroidal modes. It should be noted that the structure coefficients for surface-wave equivalent modes and coefficients in the expansion of phase velocity maps are not independent data. Indeed, for large harmonic degree, we find excellent agreement between structure coefficients estimated from travelling- and standing-wave analyses which gives us confidence in both data sets.

Given the interest in 3D density, it is useful to perform an inversion using the mode data alone. This inversion is parameterized by 18 shells in the mantle with shear velocity and bulk sound velocity expanded in spherical harmonics of degree 2,4, and 6. We scale perturbations in density to be proportional to perturbations in shear velocity. The resulting model is shown in Fig. 10 where it is clear that the bulk sound speed becomes increasingly negatively correlated with the shear velocity as one goes deeper in the mantle. This is a feature of all our joint inversions (see below). The model shown in Fig. 10 gives an excellent fit to the mode data and has an overall χ^2/N of 0.9 with no systematic misfit of any mode branch. Clearly, our current mode data set can essentially be fit with the assumption that density is proportional to

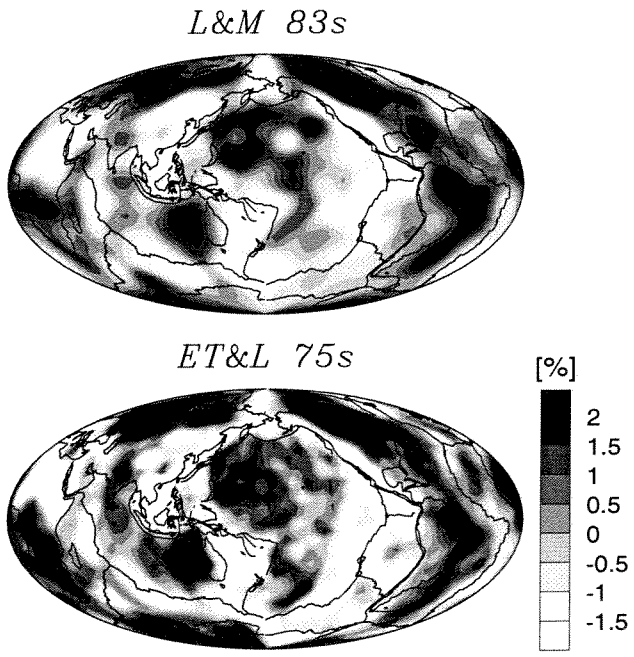

Figure 7. Phase velocity maps for Rayleigh waves at a frequency of about 12 mHz. We show maps of phase velocity perturbation with respect to the spherical average for two groups: L&M, *Laske and Masters* [1996]; and ET&L, *Ekström et al.* [1997]. At large scales, the maps are remarkably similar and show the typical features: seismically fast continental shields and old oceans and slow mid-ocean ridges. The perturbations are given in percent.

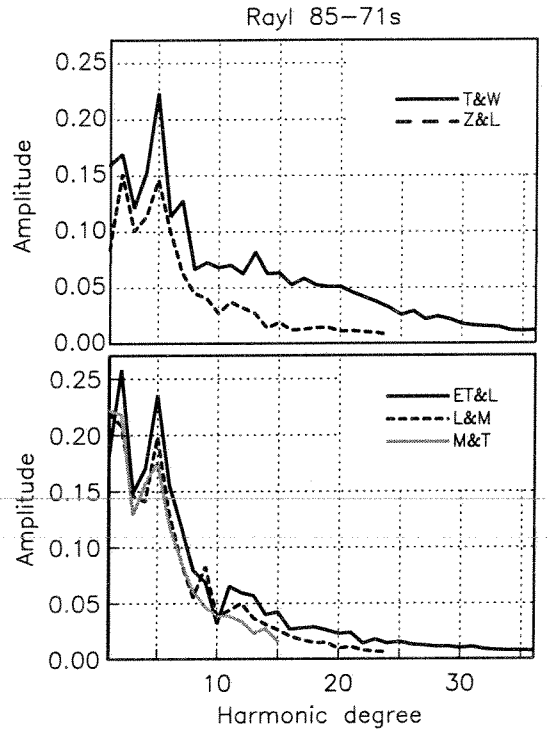

Figure 8. Amplitude spectra for Rayleigh wave phase velocity maps at around 12 mHz. The maps are: ET&L: *Ekström et al.* [1997] (75s); L&M: *Laske and Masters* [1996] (83s); T&W: *Trampert and Woodhouse* [1996] (80s); M&T: *Montagner and Tanimoto* [1990] (71s); Z&L: *Zhang and Lay* [1996] (85s).

shear velocity. This result contradicts that of *Ishii and Tromp* [1999] who find that density is negatively correlated with shear velocity in the lower mantle. To see if such a model is possible, we inverted the mode data again but now with the assumption that density is proportional to bulk sound speed (with a scaling corresponding to an Anderson-Grüneisen parameter, δ_S, of 2.5). Because the recovered bulk sound speed is still negatively correlated with shear velocity in the lower mantle, this model implicitly has a density that is also negatively correlated with shear velocity – now in agreement with the results of *Ishii and Tromp* [1999]. Futhermore, this model fits the mode data almost as well as the model with density proportional to shear velocity.

We take these results to imply that the current mode data set cannot distinguish between models in which density is positively or negatively correlated to shear velocity in the lower mantle (see also *Resovsky and Ritzwoller* [1999]). A further improvement in the precision of the structure coefficients will be required before 3D density can be resolved. The mode data do however robustly establish that bulk sound speed is negatively correlated with shear velocity in the lowermost mantle – at least at long wavelengths.

4. A HIGH-RESOLUTION INVERSION FOR SHEAR VELOCITY

We begin by inverting the long-period shear wave data sets, surface waves and structure coefficients described above for a so-called "high-resolution" shear-wave model of the mantle. This model is parameterized by 18 layers of roughly 100 km

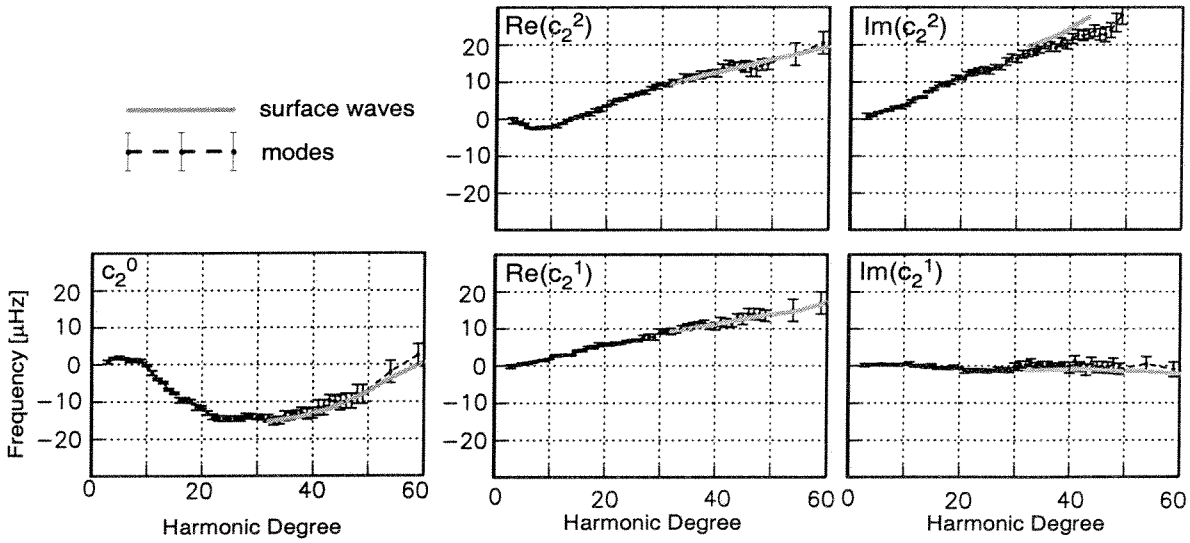

Figure 9. Degree 2 structure coefficients for fundamental spheroidal modes. The solid lines are estimates made from travelling wave studies at high harmonic degree. The agreement with the mode estimates is excellent.

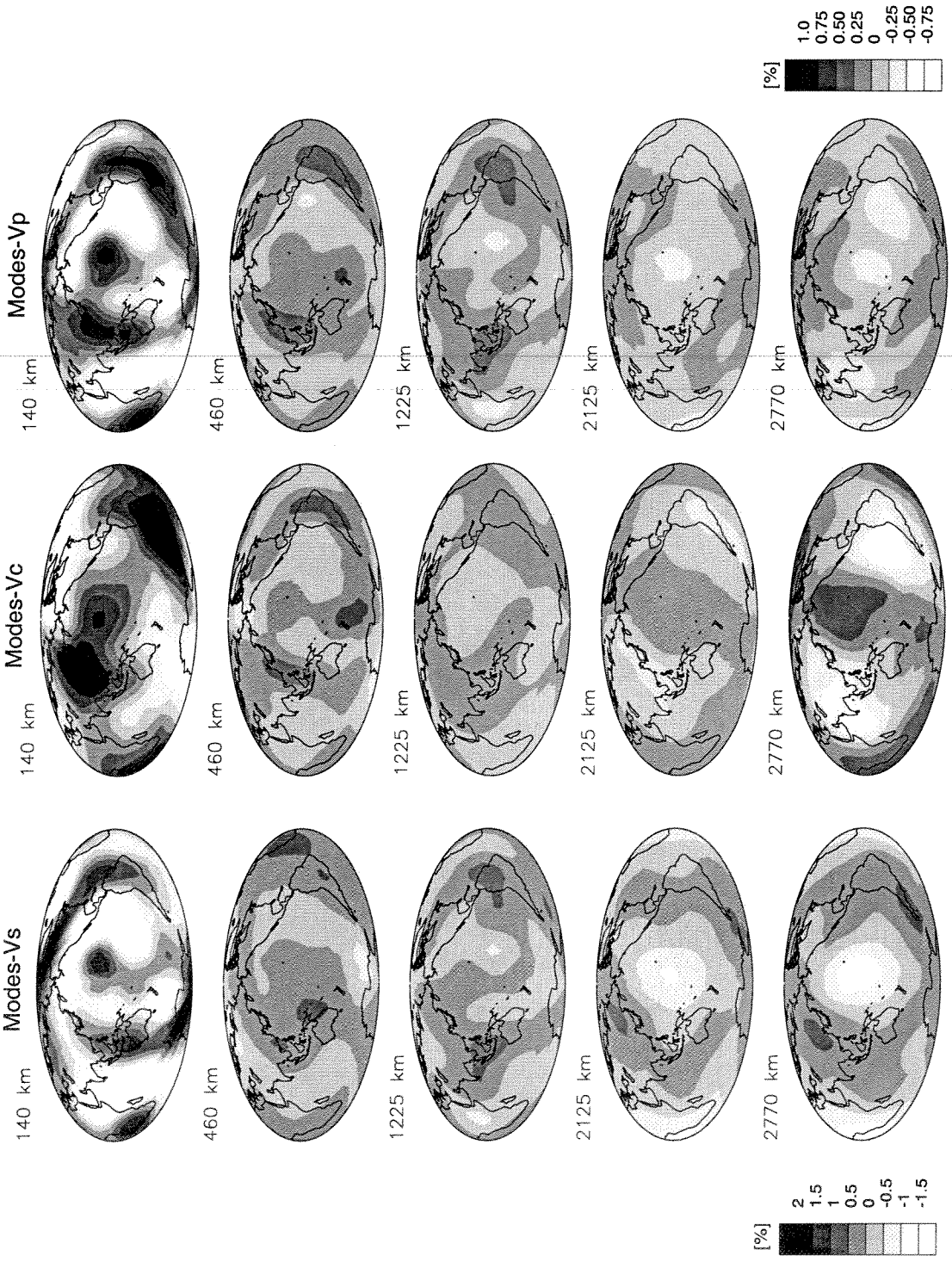

Figure 10. Cross-sections of the Earth at various depths showing perturbations of shear velocity, v_s, bulk sound speed, v_c, and compressional velocity, v_p (in percent). This model was constructed using the mode-structure coefficients alone. Note the strong anticorrelation of the bulk sound speed and shear velocity near the base of the mantle. The scale for v_c is the same as that of v_p.

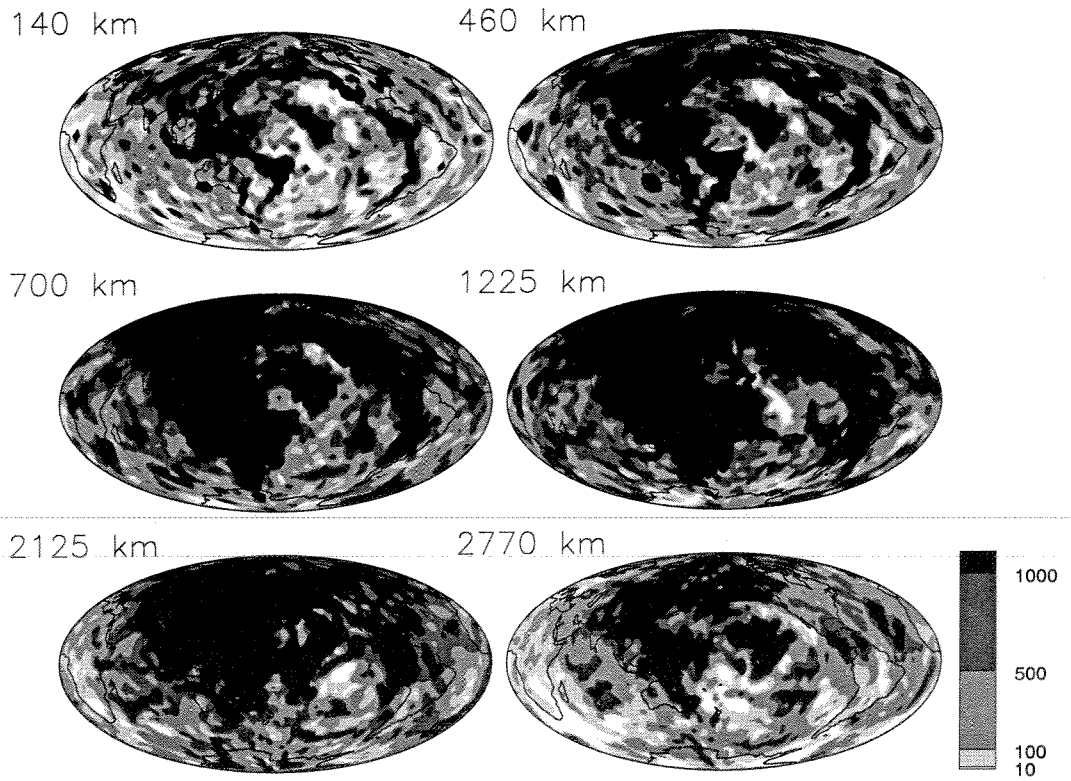

Figure 11. A graphical representation of the matrix connecting shear velocity perturbations to absolute and differential shear travel time data sets. Darker greays represent better sampling. Note that some parts of the lowermost mantle in the southern hemisphere remain poorly sampled.

thickness in the upper mantle and transition zone and 200 km thickness in the lower mantle. Each layer is divided into equal-area blocks of dimension 4 degrees at the equator. Such a model has about 46,000 model parameters. This is many less than the number of data we are employing but there are still regions of the model that are not well sampled.

Fig. 11 shows how much each block is sampled by the body waves in the inversion. Bearing in mind that the surface waves constrain well the structure in the upper mantle, we find that the only poorly sampled regions are parts of the southern hemisphere in the lowermost mantle. The recent expansion of the global seismic network may allow us to fill these holes (our data sets include events from 1976 to 1994) but their present existence should be borne in mind when interpreting the results.

Earthquake mislocation is a major source of error in our datasets and it is important to treat this properly in the inversion. This is particularly true of teleseismic P data where mislocation effects are similar in size to the signal from 3D structure (a typical mislocation error is about 0.9 sec but the signal from 3D structure is only about 1 sec) but is less important for S waves. We handle mislocation by projecting the data for each event to make linear combinations of the original data which are, to first order, insensitive to the location of the event [e.g. *Masters et al.*, 1996]. Consider a vector of travel-time residuals for an event, $\delta\mathbf{t}$:

$$\delta\mathbf{t} = \mathbf{A} \cdot \delta\mathbf{h} + \mathbf{B} \cdot \delta\mathbf{v} \tag{9}$$

where $\delta\mathbf{h}$ is a four vector describing a perturbation in location and origin time of the event, and $\delta\mathbf{v}$ is a vector of velocity perturbations describing the 3D velocity structure. We operate on the equation above with a projection matrix $\mathbf{P}$ chosen so that $\mathbf{P} \cdot \mathbf{A}$ is zero and the covariance matrix of the projected data $\mathbf{P} \cdot \delta\mathbf{t}$ is diagonal (so that the projected data are independent). This results in the loss of four data per event. We now have to solve the system

$$\mathbf{P} \cdot \delta\mathbf{t} = \mathbf{P} \cdot \mathbf{B} \cdot \delta\mathbf{v} \tag{10}$$

This process is somewhat extreme as it also projects out all structure which can be modeled by an equivalent shift in the source. We have found, however, that the results of S inversions vary little if we do the projection or not so the effects of mislocations are not dominant. (The same is not true for P inversions where the projection step can lead to quite different inversion results.)

Our inversions employ the LSQR algorithm as described by *Nolet* [1987] and we include first-difference smoothing both radially and laterally. There has been some controversy about the use of iterative inversion algorithms in seismic tomographic problems. Both SIRT [*Dines and Lytle*, 1979] and LSQR have been used in the geophysical literature though our experience has been that LSQR performs very well. As in any inversion, iterative techniques perform better when the system is well-constrained. Some recent inversions have attempted to recover over 250,000 block parameters with as little as 16,000 data. Such systems tend to converge poorly and, naturally, the results are a strong function of the smoothing employed. With the data sets at hand and our choice of parameterization, we have many more data than unknowns and convergence of the inversion is quite rapid and fairly insensitive to the degree of smoothing. In tests using synthetic data, we have found that the solution grows in amplitude and gradually asymptotes to the correct value as we iterate further. However, even after a few hundred iterations, it is possible for amplitudes near the bottom of the mantle to be slightly underestimated. This should be borne in mind when interpreting the results.

We show the results of two modeling experiments to highlight the importance of including surface-wave data. Plate 1 shows the result of fitting the long-period body-waves only and is reminiscent of many models found by inverting ISC data. Plate 2 shows the effect of including the surface waves which demand high amplitude structure in the upper mantle. It is remarkable that the presence of this structure does not really change the picture in the lower mantle where slab-like features are readily apparent. In fact, both models fit the body-wave data about equally well though only the latter model provides an acceptable fit to the surface-wave and free-oscillation data. We can conclude two things from this experiment – the first is that surface waves should be included to get reasonable results in the upper mantle, the second is that the pattern of slab-like features imaged in the lower mantle is remarkably robust.

Fig. 14 compares the amplitudes in our model with those of the recent model by *Grand* [1994] and also shows the correlation between the two models (Fig. 16). The correlation is remarkably good in both the upper and lowermost mantle but is poorest in the transition zone. Furthermore, the amplitudes in the Grand model in the middle mantle and transition zone are extremely small.

Clearly, it is important to know which (if either) model is correct if we are to start interpreting the physical cause of the anomalies we image. We currently favor the larger amplitudes of our model for the following reasons:

1) The surface wave data are underpredicted by the Grand model, particularly at low frequencies where sampling of the transition zone is strongest (see Fig. 22).

2) Our differential travel time data are poorly fit by the Grand model (Table 2) including the $ScS - S$ which are dominantly sensitive to the lower mantle.

3) Inversions of structure coefficients result in models with the larger amplitudes [see also *Resovsky and Ritzwoller*, 1998].

4) Inversions of synthetic data constructed from the Grand model using our ray geometry reproduce its low amplitudes. This suggests that our data coverage and quality are sufficient to distinguish between the models.

Clearly, we need to clarify why seismologists can generate models of such different amplitudes (even though the shapes tend to be well-correlated). The first order of business is to ensure that the data sets that go into the different inversions are compatible and this is the subject of ongoing research.

Fig. 12 shows an image of our "high-resolution" model (courtesy of Paul Tackley) which elucidates its general features – notably the large-scale low-velocity regions in the lower mantle surrounded by slab-like structures. It is also interesting to note that the "slabs" in this image do not appear to fade out a few hundred kilometers above the CMB which is a feature of some tomographic models and has been the subject of some speculation in the recent literature [*van der Hilst and Karason*, 1999].

5. JOINT INVERSION OF THE P AND S DATA SETS

5.1. Constrained Inversions

There have been many recent attempts to jointly invert for shear velocity and bulk sound speed, or shear velocity and compressional velocity. These vary in sophistication and complexity with the simplest inversions assuming that v_p and v_s anomalies have the same geographic pattern but that their relative amplitudes are allowed to vary as a function of depth. Both ISC [*Robertson & Woodhouse*, 1996] and long-period data (including surface waves) [*Bolton*, 1996] have been treated in this fashion. Contamination of the S residuals by SKS is severe for the ISC data beyond 80° so the *Robertson & Woodhouse* [1996] analysis ends at a depth of 2000km. They also confine attention to long-wavelength models of structure (spherical harmonic degree 6). Their results indicate a linear dependence of R on depth between 600km and 2000km with R ranging between from 1.7 to 2.5 (Fig. 13). The Bolton study was very similar in that long-wavelength structure was sought (up to harmonic degree 8) but now the whole mantle could be analyzed because of the use of hand-picked S arrivals from transverse components. His results are also shown in Fig. 13 along with the estimates from the crude analysis of the raw data we obtained from Fig. 4. It is remarkable how consistent a picture these different studies give and all agree that R increases monotonically in the lower mantle to a value that can not be explained by subsolidus thermal effects.

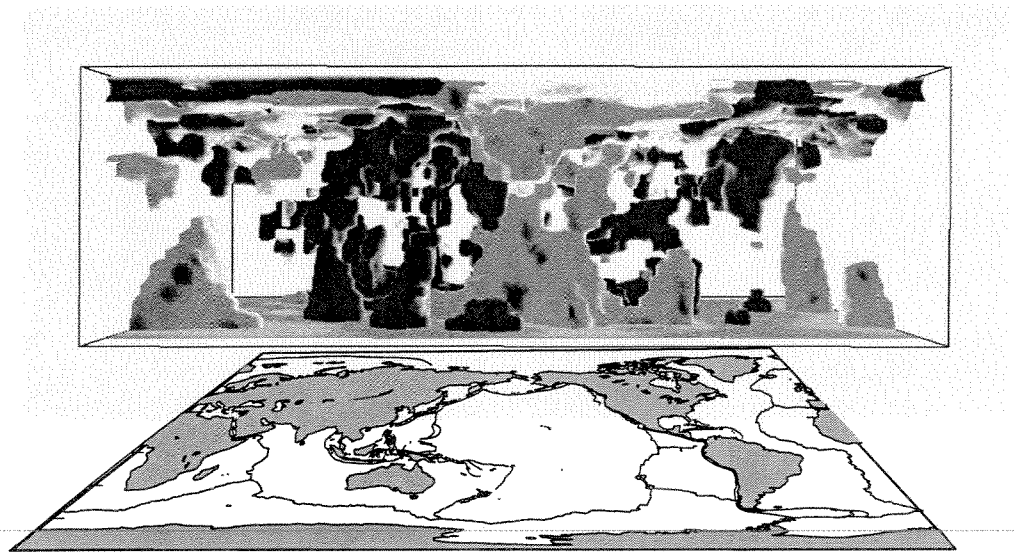

Figure 12. Isovelocity surfaces for values of -1.0% (light) and +0.6% (dark) reveal the general nature of the high resolution model SB4L18 (Plate 2): large-scale low velocity regions surrounded by fast slab-like regions which extend across the whole mantle. (Graphics courtesy of P. Tackley).

However, we are hesitant to accept these large global values of R at face value. It seems clear that the increase in R is associated with the regions in the lower mantle where there are very large (negative) v_s anomalies accompanied by much smaller v_p anomalies. These regions actually seem to be quite localized (Fig. 3) though they are usually some of the best sampled (e.g. the central Pacific) which might lead to bias in the inversion. We therefore now turn attention to inversions where the geographic shapes of the velocity anomalies are not required to be the same.

5.2. *Unconstrained Inversions*

For the purposes of this paper, we have performed a joint bulk sound speed - shear velocity inversion of the data sets described above. In the interests of computational expediency, we have parameterized both velocities by a mantle divided into 18 layers each of which is divided into equal area blocks of dimension 10 degrees at the equator (this is equivalent to a spherical harmonic expansion of about harmonic degree 20). Again, we employ the LSQR algorithm and we include first-difference smoothing both radially and laterally.

The reason for the relatively coarse parameterization is that we must now perform the earthquake-location projection step to obtain reliable P models. When we have many data (both P and S) per event, the projected data are each linear combinations of *all* the original data and can sample a significant fraction of the model. This makes the matrices significantly less sparse and the inversion becomes much more of a computational burden.

Our favorite joint model is shown in Plate 3 (SB10L18) and the fit of this model to our data is shown in Table 2. The amplitude of this model is compared with others in Fig. 14. This model demonstrates a robust feature of all joint models we have obtained: the correlation between the bulk sound speed and the shear velocity becomes negative in the lowermost mantle (Fig. 15). This feature was first noted by *Su & Dziewonski* [1997] though their negative correla-

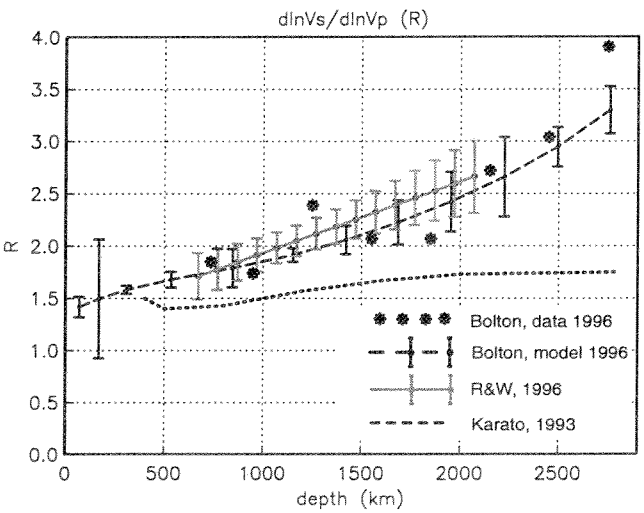

Figure 13. $R = dlnv_s/dlnv_p$ for two joint models which assume that the geographical shape of the compressional velocity anomaly is perfectly proportional to the shape of the shear velocity anomaly. Also shown are the values obtained directly from the data binned by ray turning depth (see Fig. 4). The resulting R values rapidly increase toward the CMB and are far too large to be explained by ordinary thermal effects [*Karato*, 1993].

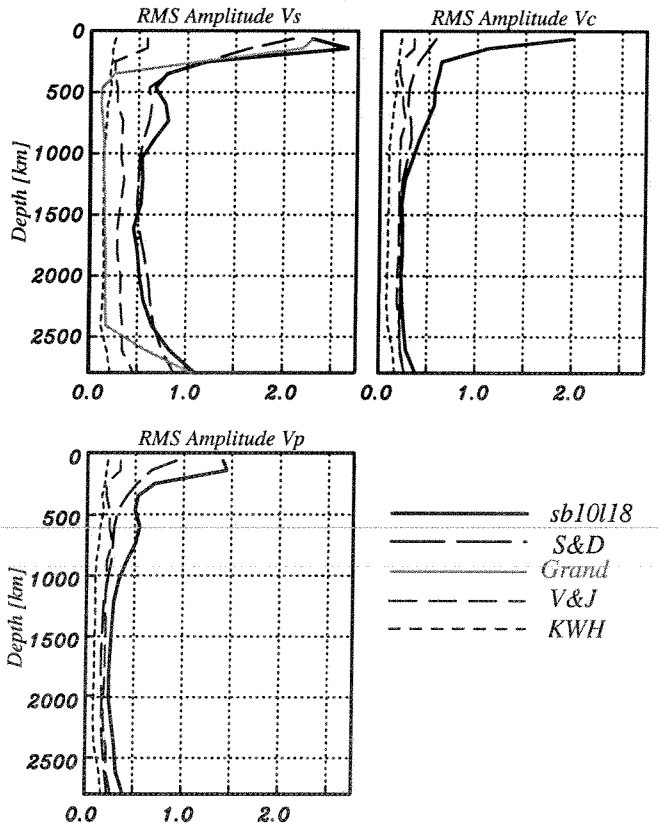

Figure 14. RMS amplitudes of shear and compressional velocities and bulk sound speed for several recent models. Note how the Grand and KWH models have extremely small shear velocity amplitudes in the mid mantle which leads to disagreement with several data sets. The models are: SB10L18: this study; S&D: *Su and Dziewonski* [1997]; V&J: *Vasco and Johnson* [1998]; KWH: *Kennett et al.* [1998]; Grand: *Grand* [1994]. The amplitude of SB4L18 is almost identical to that of SB10L18.

tion is stronger and extends to shallower depths than in our model. Another feature of the joint models is that the compressional velocity is strongly correlated with the shear velocity throughout the mantle (Fig. 15). We also show the correlation between the various shear velocity models in Fig. 16.

We have also computed a spherically-averaged R value as a function of depth for this and other models. We have noticed that different authors compute R in different ways. Our choice is to take all blocks in each shell which have non-zero values of both compressional and shear velocity perturbations and take their ratio. A histogram of these pixel-by-pixel estimates is made (Fig. 17) and the median value chosen as the best value for each shell. The values that we now obtain are smaller than found in the previous section but still show the increasing trend with depth (Fig. 18, curve SB10L18). This may confirm our suspicion that some relatively local regions with extreme values of R biased the inversions of the previous section. Our spherically averaged values of R are now much more consistent with the predictions of normal thermal effects with the possible exception of the lowermost mantle.

Table 2. Fit of models to the S data sets, VR is the variance reduction in percent.

	$SS-S$		$ScS-S$		unproj. S	
Model	χ^2/N	VR	χ^2/N	VR	χ^2/N	VR
SB4L18	1.1	73	2.0	66	4.2	41
SB10L18	1.3	69	2.0	66	4.2	41
Grand	2.5	41	3.9	39	4.2	41
KWH	3.8	14	5.3	20	7.1	8
V&J	4.0	10	6.5	-1	5.7	23
S&D	2.5	42	2.9	50	4.9	34

5.3. Comparison With Other Models

We now compare four recent joint models of velocities in the mantle. Three of these are products of joint bulk sound speed/ shear velocity inversions: this inversion, SB10L18 (Plate 3); *Su and Dziewonski* 1997, (S&D, Fig. 19), and *Kennett et al.* 1998, (KWH, Fig. 20)]. One model resulted from a joint compressional/shear velocity inversion [*Vasco and Johnson*, 1998 (V&J, Fig. 21)].

All the joint v_c/v_s inversions give models for which v_p is highly correlated with v_s (Fig. 15). This seems to be a natural outcome of this parameterization while joint v_p/v_s inversions lead to much less correlation. For three models v_c is negatively correlated with v_s in at least part of the lower

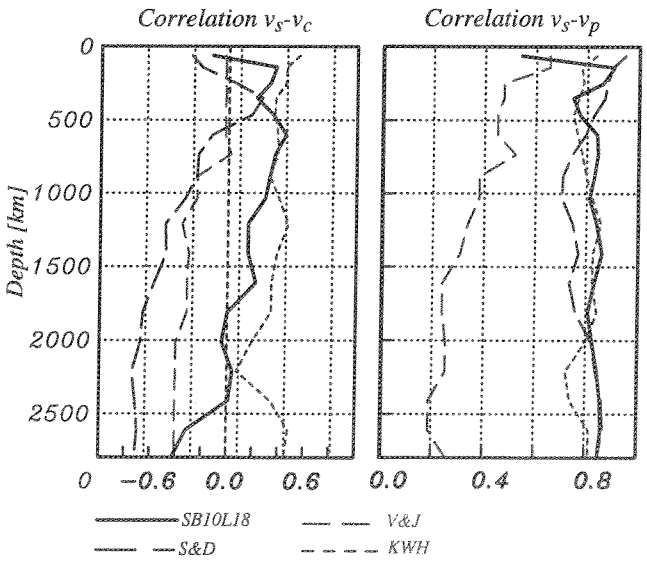

Figure 15. The correlation of v_s–v_c and of v_s–v_p as a function of depth in the mantle for a variety of models. Note that all models exhibit negative correlation for v_s–v_c near the base of the mantle except for model KWH.

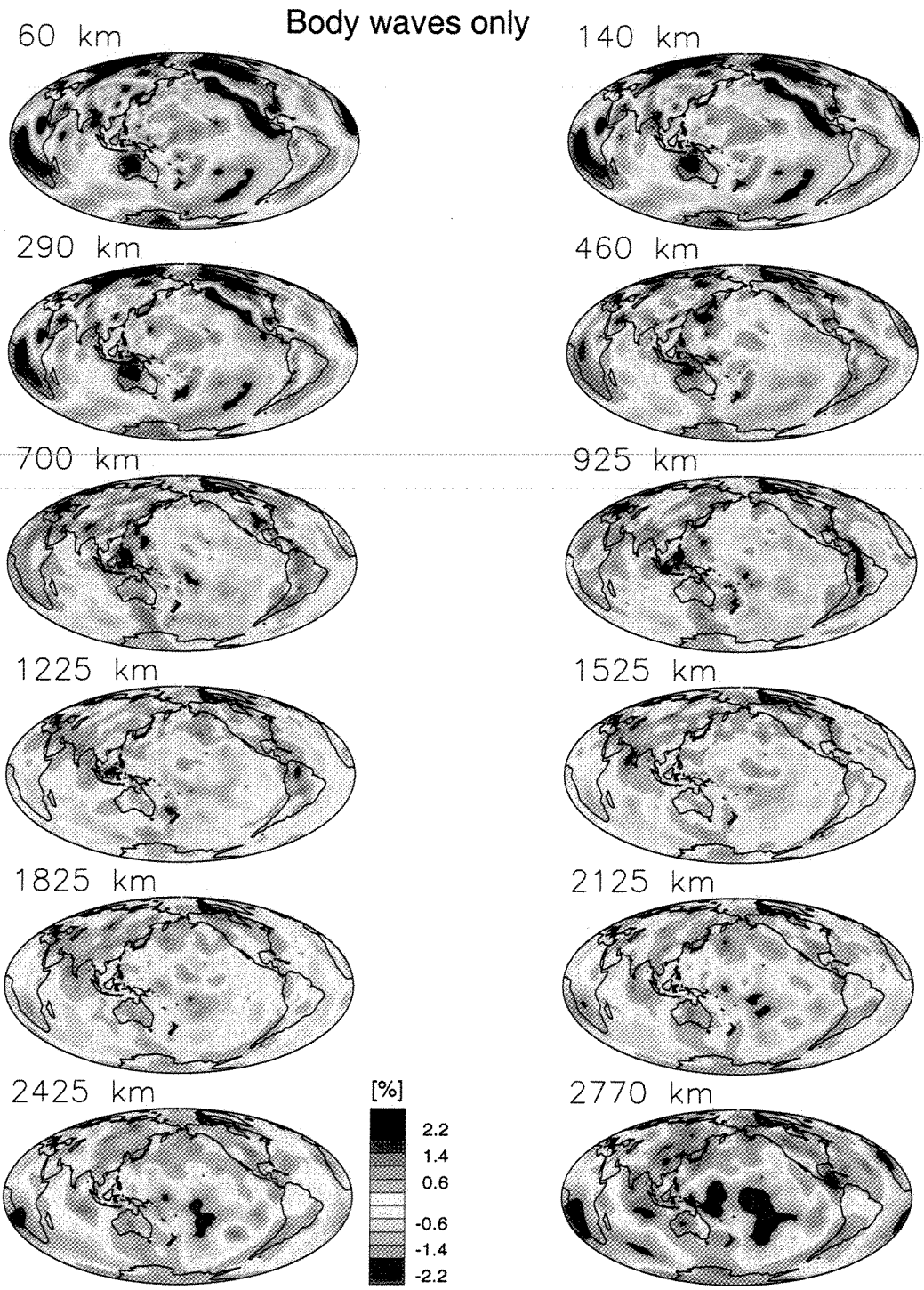

Plate 1. Cross-sections of the Earth at various depths showing perturbations of shear velocity (in percent). This high-resolution model was constructed using body wave data alone.

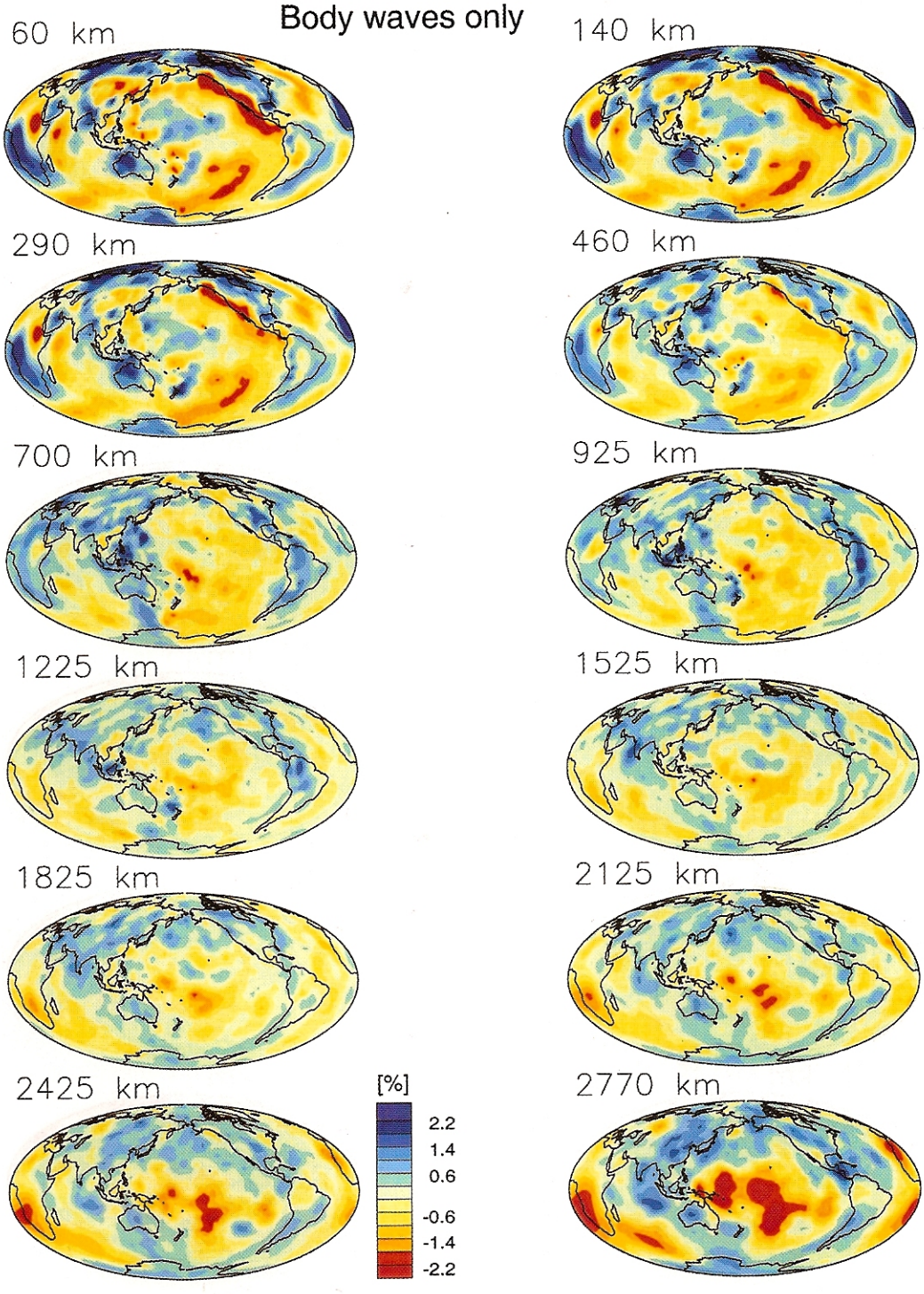

Plate 1. Cross-sections of the Earth at various depths showing perturbations of shear velocity (in percent). This high-resolution model was constructed using body wave data alone.

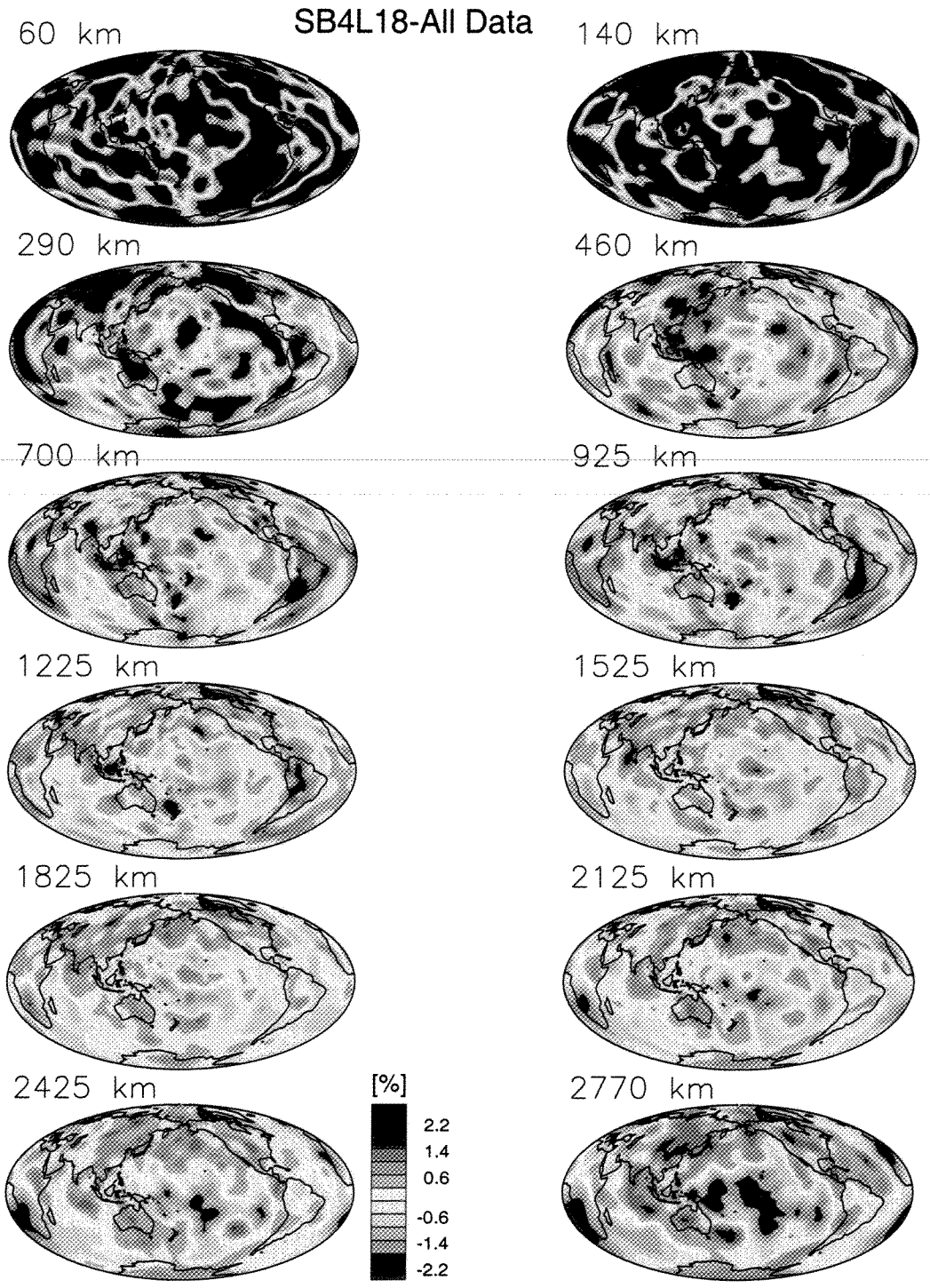

Plate 2. Cross-sections of the Earth at various depths showing perturbations of shear velocity (in percent). This high-resolution model (SB4L18) was constructed using surface-wave and free-oscillation data as well as body wave data. Compare with Plate 1. Note that the upper mantle is completely different but the anomalies in the lower mantle appear to be remarkably similar.

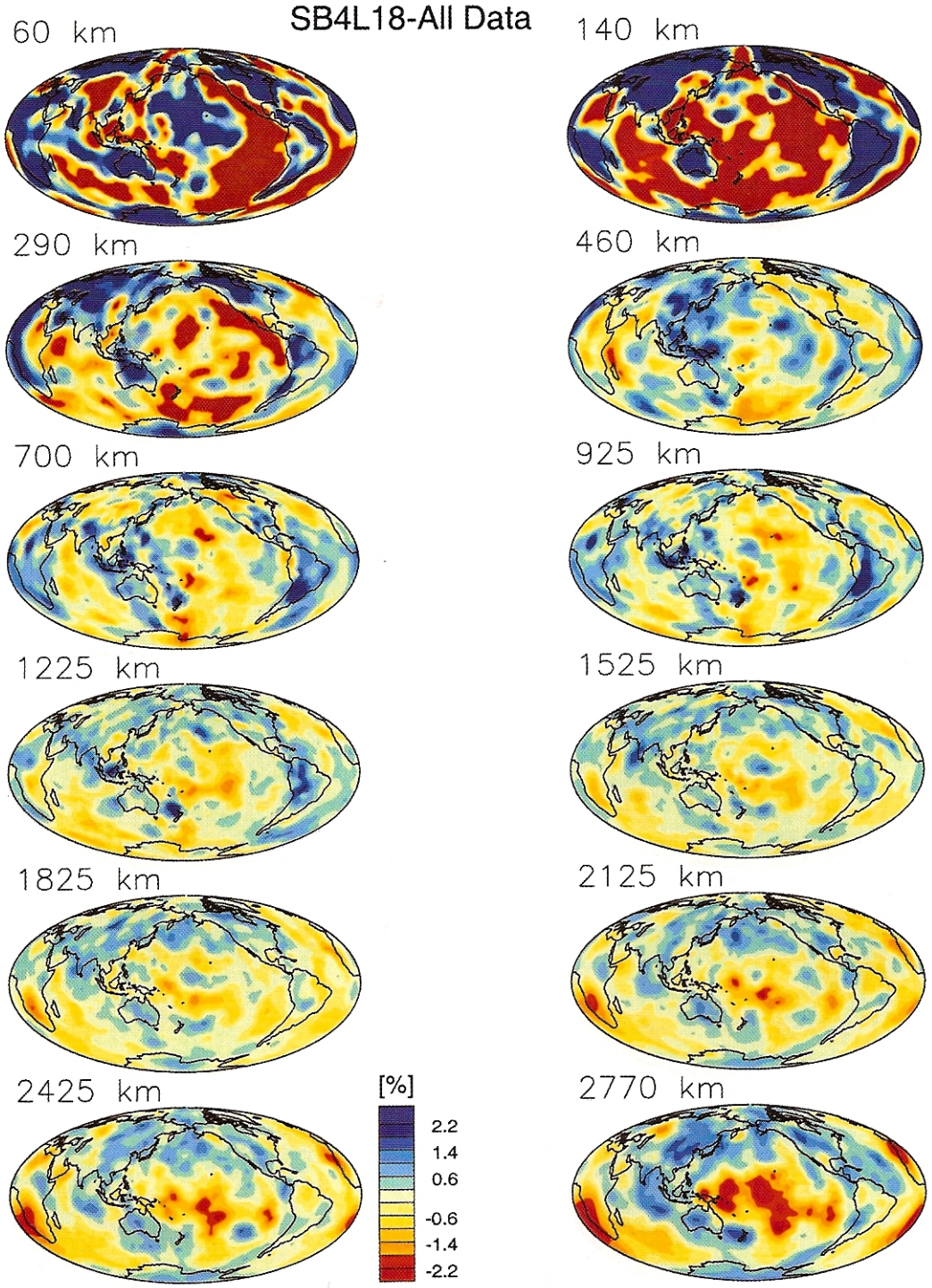

Plate 2. Cross-sections of the Earth at various depths showing perturbations of shear velocity (in percent). This high-resolution model (SB4L18) was constructed using surface-wave and free-oscillation data as well as body wave data. Compare with Plate 1. Note that the upper mantle is completely different but the anomalies in the lower mantle appear to be remarkably similar.

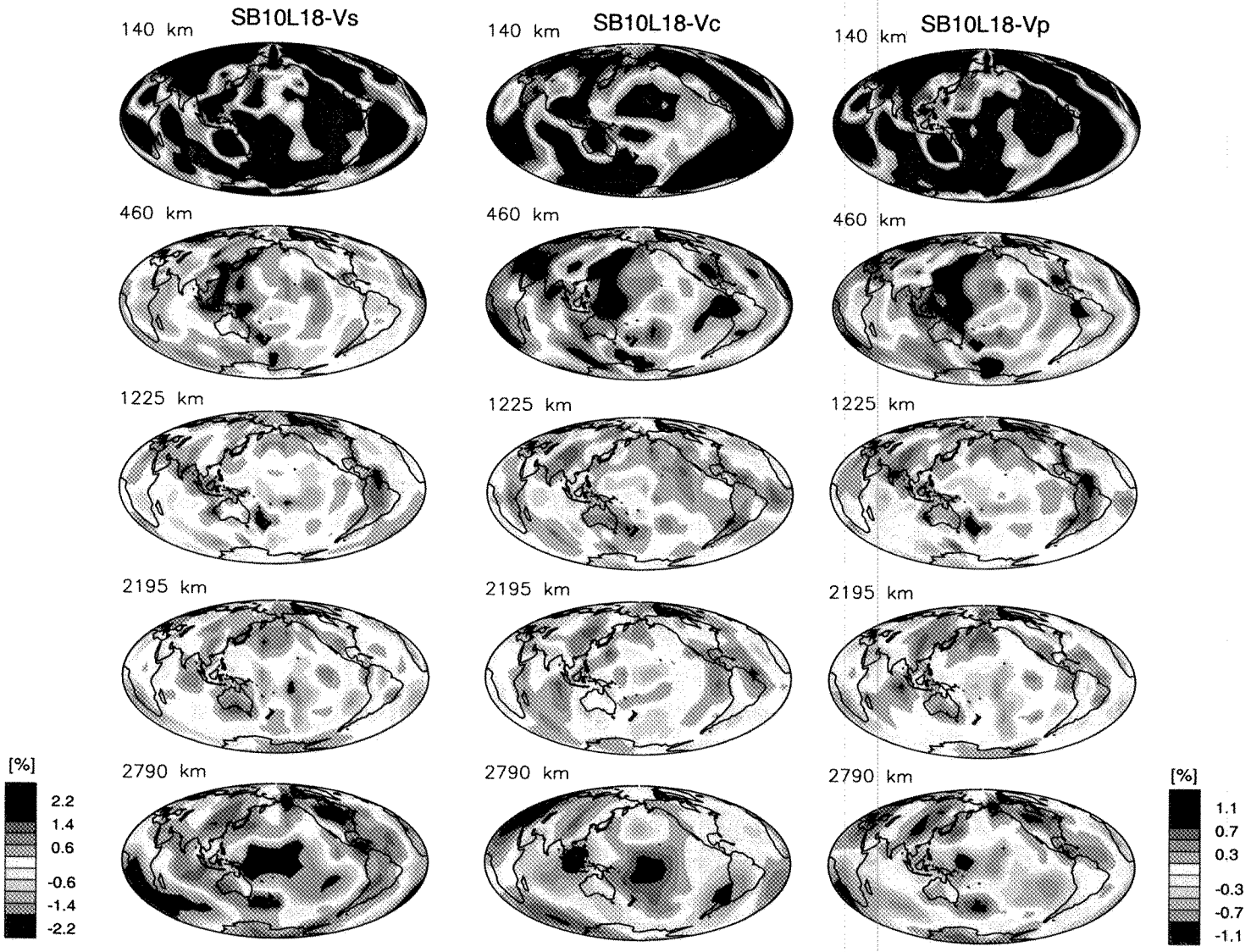

Plate 3. Cross-sections of the Earth at various depths showing perturbations of shear velocity, bulk sound speed and compressional velocity (in percent). This jointly-inverted model (SB10L18) was constructed using surface-wave and free-oscillation data as well as body wave data. Note the anticorrelation of bulk sound speed with shear velocity near the base of the mantle. Compressional velocity is strongly correlated with shear velocity throughout the mantle. The color scale for v_c is the same as that of v_p.

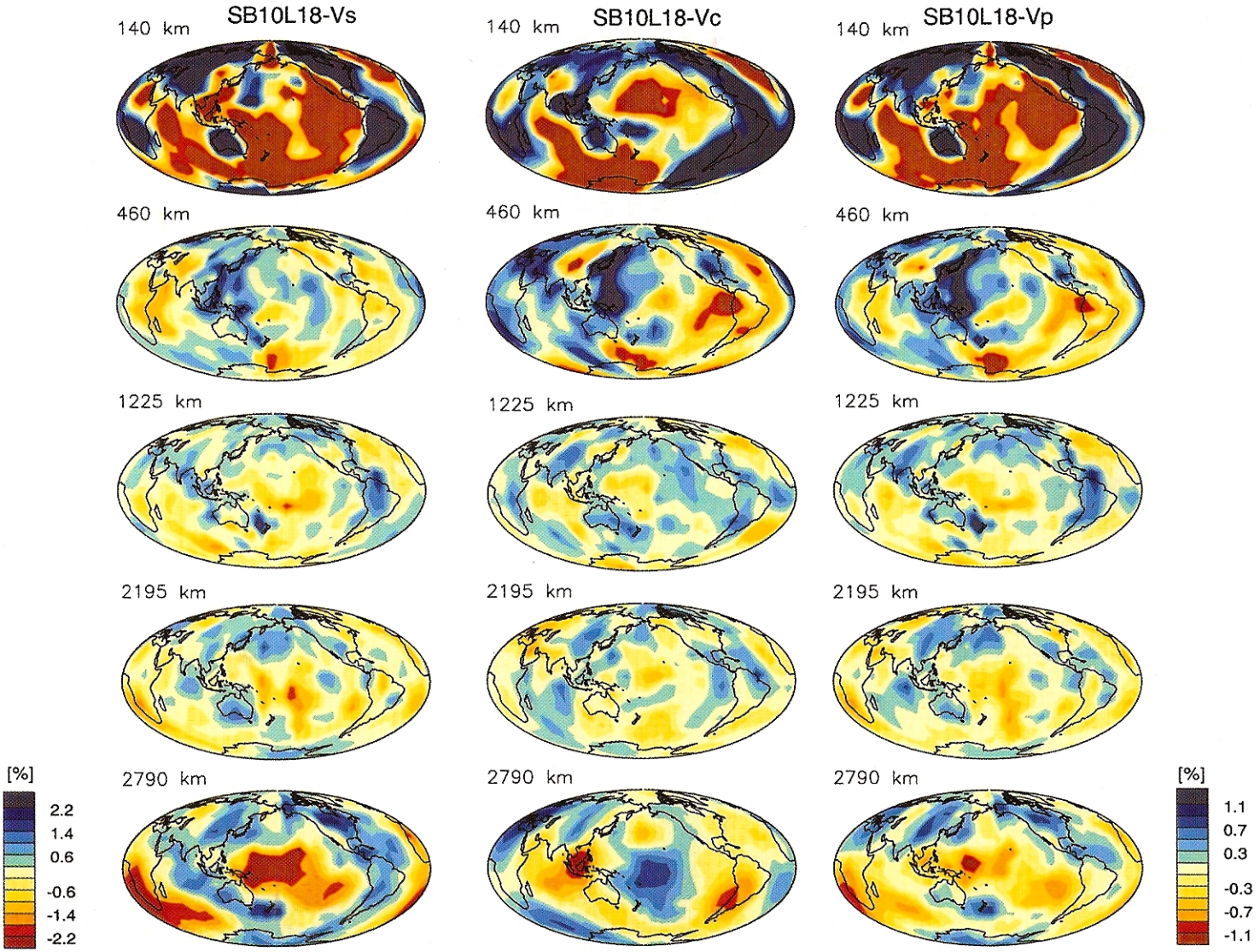

Plate 3. Cross-sections of the Earth at various depths showing perturbations of shear velocity, bulk sound speed and compressional velocity (in percent). This jointly-inverted model (SB10L18) was constructed using surface-wave and free-oscillation data as well as body wave data. Note the anticorrelation of bulk sound speed with shear velocity near the base of the mantle. Compressional velocity is strongly correlated with shear velocity throughout the mantle. The color scale for v_c is the same as that of v_p.

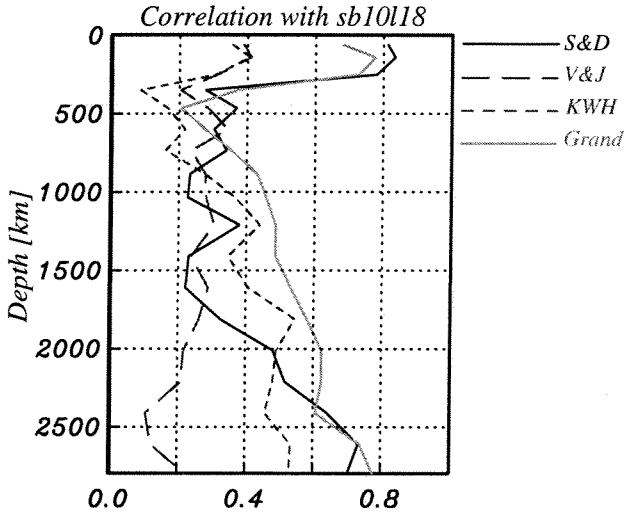

Figure 16. The correlation for v_s of SB10L18 with other models, as a function of depth. Note the excellent correlation of SB10L18 with S&D and Grand in the upper mantle. The correlation is significantly decreased in the lower mantle but rises towards the bottom. Also note that SB10L18 and the V&J model correlate poorly at all depths.

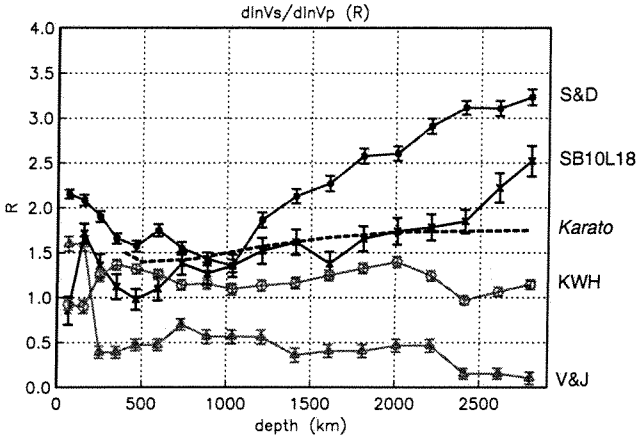

Figure 18. $R = dlnv_s/dlnv_p$ for the four unconstrained joint models. Model S&D gives answers very similar to the constrained inversions. Model SB10L18 shows a more modest increase of R across the mantle. The remaining two models show much smaller values of R.

mantle. The exception is model KWH where v_c is positively correlated with v_s throughout the whole mantle.

There is a wide variety in the behavior of R with depth. Both S&D and SB10L18 show a general increase of R with depth (Fig. 18) with the values of S&D being very similar to those determined from the unconstrained inversions. It is interesting to note that S&D use a degree 12 spherical harmonic expansion which is significantly more constrained than the parameterization of SB10L18 and which might partly contribute to the difference. S&D and SB10L18 also have very similar amplitudes for the anomalies in the mantle (Fig. 14) which might be partially explained by the fact that both of these models are built using surface wave and long-period body waves data sets though S&D also include ISC P data. The two models based on ISC data, KWH and V&J, are very different from the previous two models and quite different from each other. In particular, the amplitudes of the shear anomalies in the KWH model are extremely small and the V&J shear model does not correlate with other models in the lower mantle.

We would obviously like to be able to distinguish which, if any, of these models has the correct levels of heterogeneity

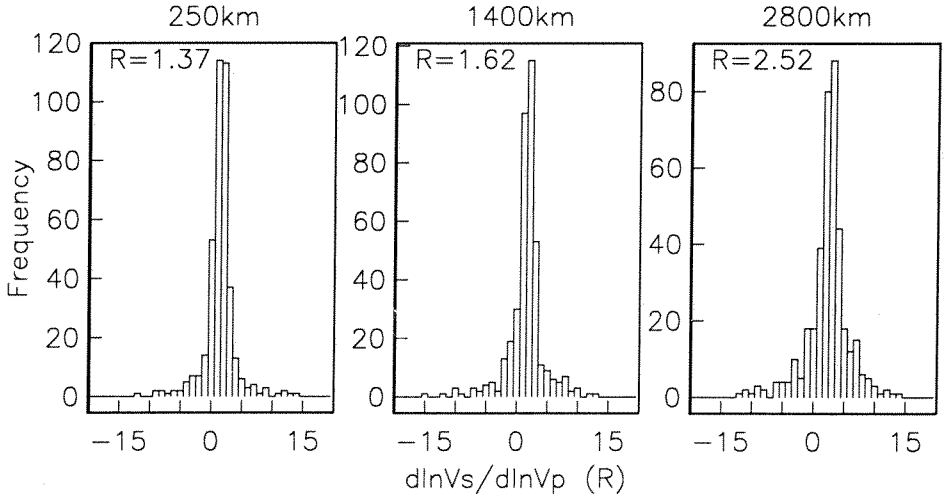

Figure 17. Histograms of R computed pixel-by-pixel at various depths in the mantle. This example is for model SB10L18 and we show R near the top, center, and base of the mantle. The mean value is quite robust and is used as an estimate of the spherically averaged value of R.

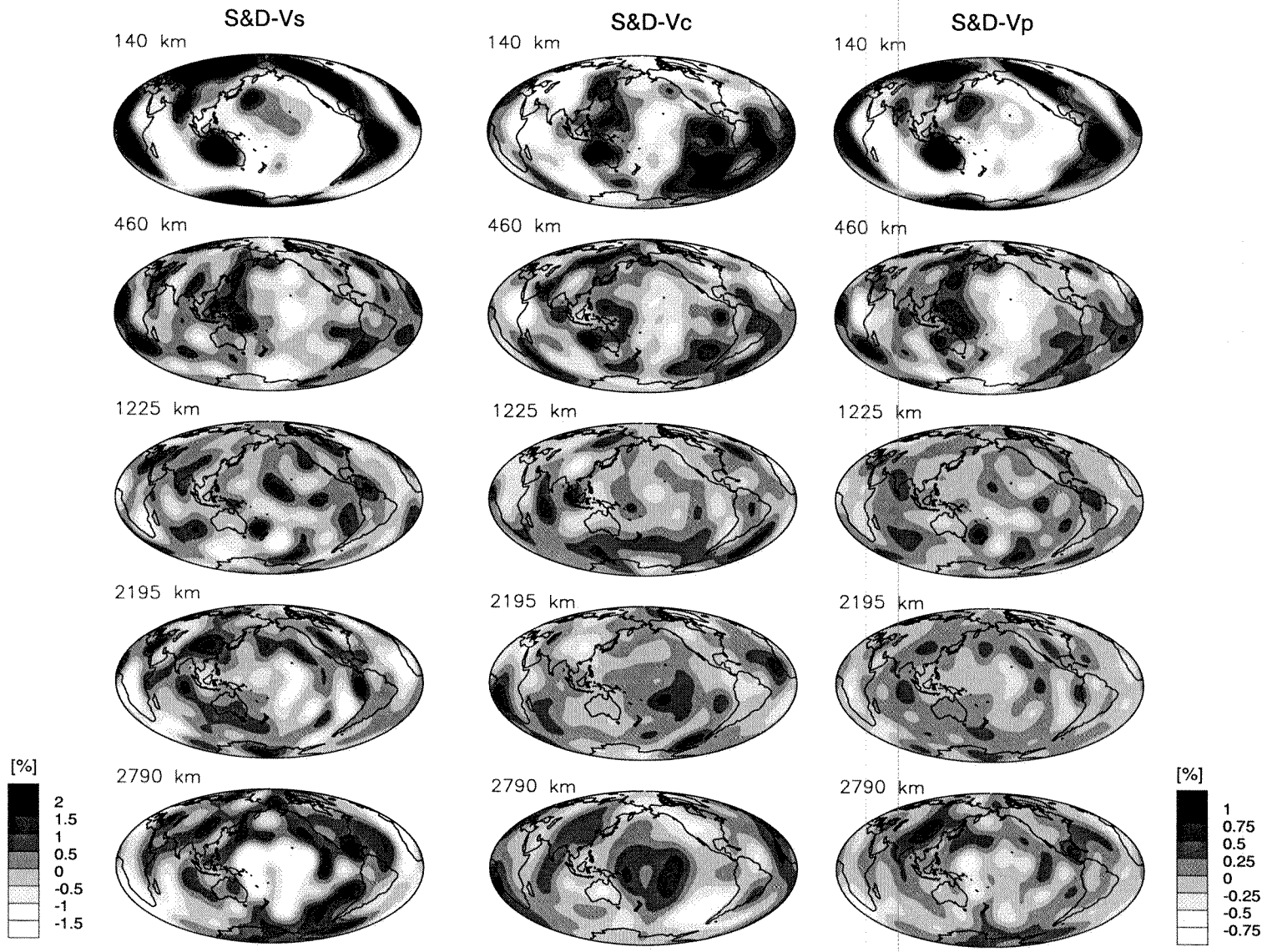

Figure 19. Cross-sections of the S&D model. For details see caption to Plate 3. Note the anticorrelation of bulk sound speed with shear velocity near the base of the mantle.

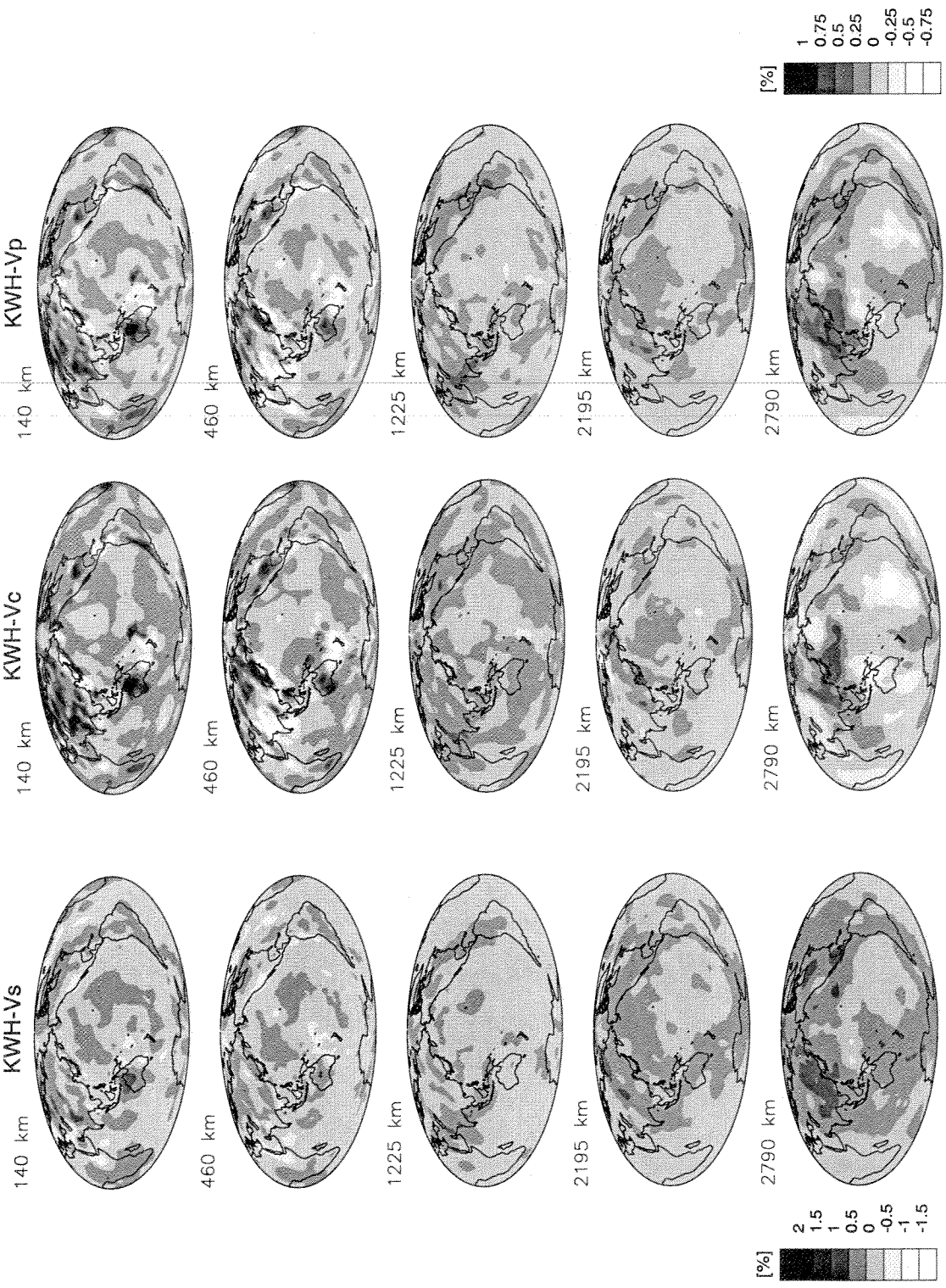

Figure 20. Cross-sections of the KWH model. For details see caption to Plate 3.

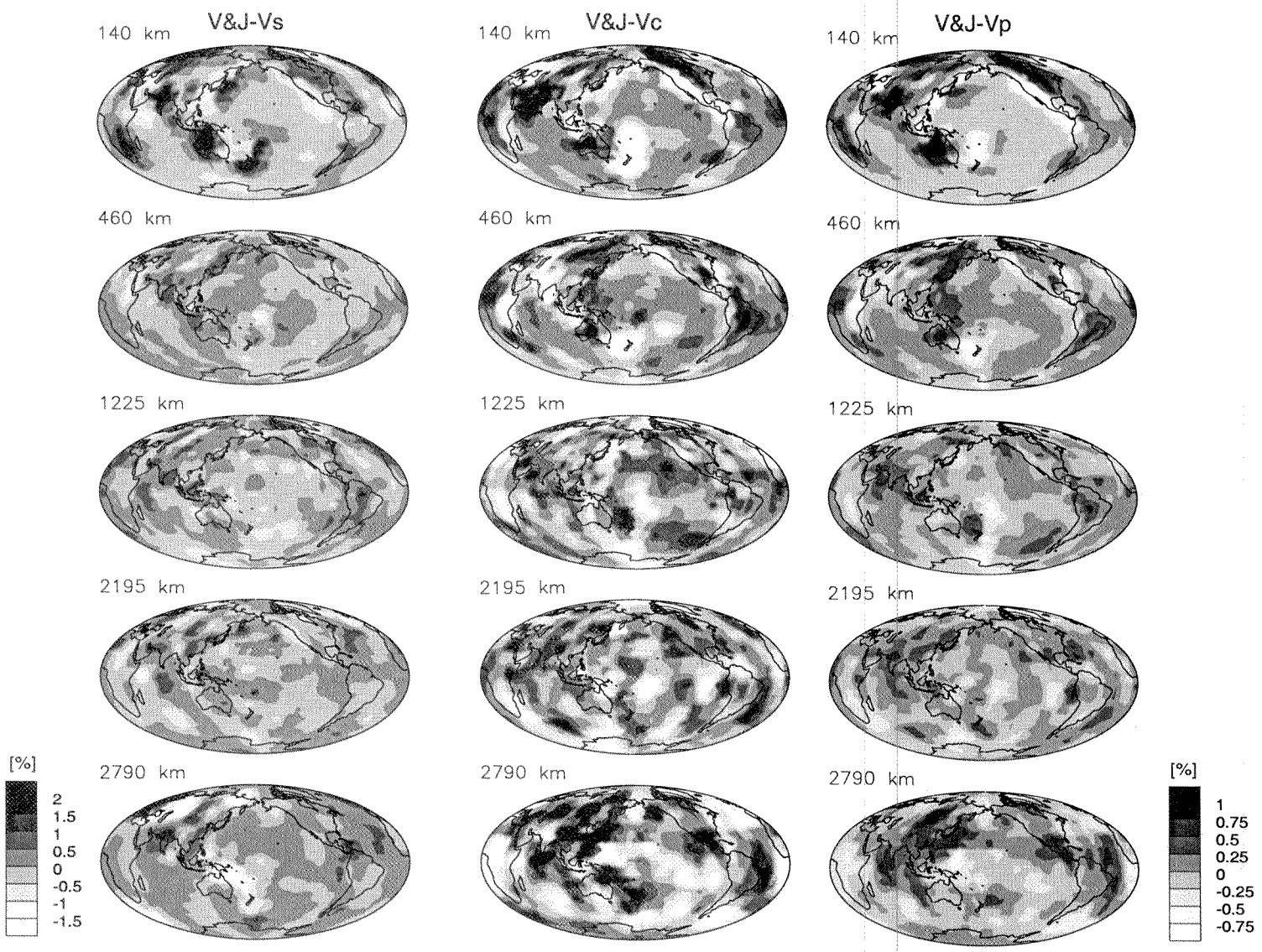

Figure 21. Cross-sections of the V&J model. For details see caption to Plate 3.

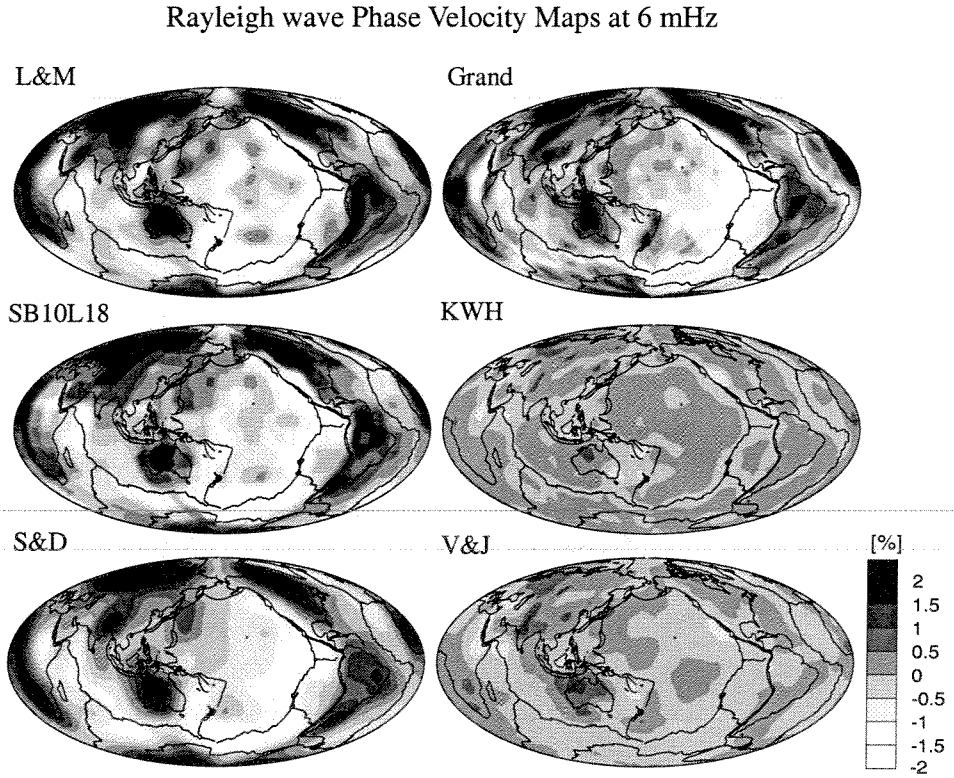

Figure 22. The phase velocity maps for Rayleigh waves at 6 mHz as predicted by the models discussed in this study. The L&M map is the measured map of *Laske and Masters* [1996]. Note the good agreement between predicted and observed maps for the models SB10L18 and S&D. Agreement is also quite good for the model of Grand though the amplitude is somewhat underestimated.The phase velocity variations are with respect to the spherical average and are given in percent.

in the mantle. This is quite difficult to do since the ISC-based models have incomplete upper mantles (due to poor data coverage). We therefore cannot quantify a comparison of model predictions with many of the global data sets such as mode structure coefficients. Here, we rather rely on a visual comparison of predicted and measured data. Fig. 22 shows Rayleigh wave phase velocity maps for 6 mHz as predicted by the models discussed here and the Grand model discussed in section 4. For the Grand model, the standard scalings were adopted to create the map ($dlnv_s/dlnv_p = 1.7$, $dlnv_s/dln\rho = 2.5$). We see that his model (as well as the two joint $v_s - v_c$ models that included surface waves in the modeling process) can reproduce the basic features of such maps. Obvious differences are: the S&D model produces smoothed phase velocity maps due to the $\ell = 12$ truncation of the spherical harmonic expansion and SB10L18 produces "blocky" maps due to the relatively large block size. It is interesting to note that the amplitudes in the maps for both Rayleigh and Love waves predicted by Grand's model tend to be too small for very long periods (around 6mHz and below). This is probably caused by the rapid decrease of the rms amplitude of Grand's model in the transition zone (Fig. 14). The two models that did not include surface waves in the modeling process (KWH and V&J) predict phase velocity maps whose amplitudes are about an order of magnitude too small – even allowing for their restricted sampling. While the KWH model predicts the location of most long-wavelength features correctly , the V&J model predicts several features not seen in the observed maps (e.g. fast velocities around New Zealand).

A data set that can be used to check the overall level of heterogeneity in the lower mantle is the set of $ScS - S$ differential times since these are fairly insensitive to structure in the upper mantle. Not surprisingly, our model SB10L18 fits best with a 66% variance reduction, model S&D achieves a 50% variance reduction, model KWH a 20% variance reduction and model V&J a slightly negative variance reduction (Table 2). The poor performance of the last two models may reflect the difficulty of constraining S velocity in the lowermost mantle with ISC data alone (as discussed above).

6. DISCUSSION AND CONCLUSIONS

At this point, readers may be excused if they feel bewildered by the range of seismic models that we have presented.

We shall therefore try to formulate some general observations though some of our conclusions (e.g. about the behavior of R) require discounting the amplitudes of the models built primarily from ISC data.

1) Our limited comparison indicates that ISC and long-period travel time residual patterns for various stations are compatible with each other. The signal level in the ISC P data is better than for the long-period P data but the signal level in the ISC S data is much worse than in the long-period S data. The range of S residuals found in both data sets is similar (up to 15 second residuals for teleseismic S) and greatly exceeds the range used by the ISC ($\pm$7.5 sec) to identify teleseismic S. The fact that the KWH model restricted attention to S residuals smaller than 7.5 sec may have contributed to its very small amplitudes.

2) The effects of earthquake mislocation can contribute errors to arrival times which are comparable in size with the signal from 3D structure for P waves. Hence, accounting for relocation in the inversion is critical.

3) We have generally found that the results of the inversions do not depend upon the inversion technique (e.g. iterative or direct) provided that the inverse problem is not grossly ill-conditioned. Gross over-parameterization can lead to poor convergence characteristics of some iterative solvers and, naturally, a strong dependence on regularization criteria.

4) Inversions of the current structure coefficient data set do not convincingly recover 3D density structure – in particular, we can not yet say whether density is positively or negatively correlated to shear velocity in the lowermost mantle.

5) The upper mantles of models based on travel times alone tend to have seismic anomalies that are greatly underestimated in magnitude (though inclusion of multiple bounce triplication phases [*Grand*, 1994] appears to be an effective strategy to combat this). Velocity anomaly patterns in the lower mantle are surprisingly robust to the inclusion of surface wave data which can radically change the models of the upper mantle.

6) Our high resolution models have amplitudes of velocity anomalies in the mid mantle consistent with previous low-resolution models. These amplitudes are compatible with both mode-structure coefficients and differential travel time data.

7) Our models show slab-like structures that extend throughout the mantle with little "fade-out" a few hundred kilometers above the CMB (see also Fig. 14)

8) Joint modeling of either ISC P and S data or long-period P and S data assuming identical (large-scale) patterns of velocity anomalies results in estimates of $R(z)$ which are quite high and increase towards the CMB. We speculate that extremely high values of R at the base of the mantle are a result of some relatively localized regions where large S velocity anomalies are accompanied by relatively minor P velocity anomalies.

9) More general unconstrained inversions lead to models in which perturbations in bulk sound speed negatively correlate with perturbations in shear velocity in at least part of the lower mantle (SB10L18 and S&D) though even here there is some discrepancy over the depth range over which the negative correlation exists. The S&D inversion shows a negative correlation over almost all the lower mantle, the modes-only inversion (Fig. 10) shows a negative correlation for about the bottom 800km of the lower mantle, while SB10L18 has the negative correlation over only the bottom 400 km of the lower mantle. There is some suggestion that the negative correlation is strongest for the longest wavelengths which partially accounts for the discrepancy. At the present time, a mineral physicist looking for the "best" value of $R(z)$ to model should probably choose something between the curves for S&D and SB10L18 in Fig. 18.

10) In much of our analysis, we can identify a central Pacific region in the deep mantle as being particularly anomalous. The fact that this region is far from places of historic subduction is worthy of note – indeed the anomalous regions appears to be associated with a slow (warm) and presumably upwelling region in the lower mantle. Such regions also seem to be associated with ultra-low-velocity zones [ULVZ – see e.g. *Lay et al.*, 1998] which may indicate chemical interaction of the core and mantle. Perhaps entrainment of such chemical heterogeneity into the lowermost mantle (and/or partial melting associated with this chemical contamination) can give rise to the anomalous values of R that we observe.

Acknowledgments. This research was supported by grants from the National Science Foundation. We are grateful to the network operators of the IRIS/IDA,IRIS/USGS, and GEOSCOPE networks, and the IRIS DMC for collecting and making easily available the data which made this study possible. We would also like to thank Paul Tackley for providing Fig. 12.

REFERENCES

Agnon, A., and M. Bukowinski, δ_s at high pressure and $d\ln v_s/d\ln v_p$ in the lower mantle, *Geophys. Res. Lett*, *17*, 1149–1152, 1990.

Anderson, O.L., and D.G. Isaak, Elastic constants of mantle minerals at high temperature, in *Mineral Physics and Crystallography, AGU Ref. Shelf #2, ed. T.J. Ahrens*, pp.64–97, 1995.

Bijwaard, H., W. Spakman, and E.R. Engdahl, Closing the gap between regional and global travel time tomography, *J. Geophys. Res.*, *103*, 30,055–30,078, 1998.

Bolton, H., Long period travel times and the structure of the mantle, *Ph.D. Thesis, U.C.S.D., La Jolla, California*, , 1996.

Bolton, H., and G. Masters, Traveltimes of P and S from the Global Digital Seismic Networks; Implications for the Relative Variation of P and S Velocity in the Mantle, *J. Geophys. Res.*, submitted, 1999.

Clayton, R.W., and R.P. Comer, A tomographic analysis of mantle heterogeneities from body wave travel time data, *EOS Trans. AGU*, *64*, 776, 1983.

Creager, K.C., and T.H. Jordan, Large scale structure of the outermost core from P'_{DF} and P'_{AB} traveltimes, *EOS Trans. AGU*, *67*, 311, 1986.

Dines, K., and J. Lytle, Computerized geophysical tomography, *Proc. IEEE, 67*, 1065–1073, 1979.

Dziewonski, A.M., Mapping the lower mantle: determination of lateral heterogeneity in *P* velocity up to degree and order 6, *J. Geophys. Res., 89*, 5929–5952, 1984.

Dziewonski, A.M., and D.L. Anderson, Preliminary reference Earth model, *Phys. Earth Planet. Inter., 25*, 297–356, 1981.

Dziewonski, A.M., and D.L. Anderson, Travel times and station corrections for *P*-waves at teleseismic distances, *J. Geophys. Res., 88*, 3295–3314, 1983.

Dziewonski, A.M., and J.H. Woodhouse, Global images of the Earth's interior, *Science, 236*, 37–48, 1987.

Ekström, G., J. Tromp, and E.W. Larson, Measurements and models of global models of surface wave propagation, *J. Geophys. Res., 102*, 8137–8157, 1997.

Engdahl, E.R., R.D. van der Hilst, and R.P. Buland, Global teleseismic earthquake relocation with improved travel times and procedures for depth determination, *Bull. Seis. Soc. Am., 88*, 722–743, 1998.

Forte, A.M., and W.R. Peltier, Mantle convection and core-mantle boundary topography, *J. Geophys. Res., 92*, 3645–3679, 1987.

Giardini, D., X.-D. Li, and J.H. Woodhouse, Three-dimensional structure of the earth from splitting in free oscillation spectra, *Nature, 325*, 405–411, 1987.

Grand, S.P., Mantle shear structure beneath the Americas and surrounding oceans, *Journ. Geophys. Res., 99*, 11.591–11.621, 1994.

Gudmundsson, O., J.H. Davis, and R.W. Clayton, Stochastic analysis of global traveltime data: mantle heterogeneity and random errors in the ISC data, *Geophys. J. Int., 102*, 25–43, 1990.

He, X., and J. Tromp, Normal mode constraints on the structure of the Earth, *J. Geophys. Res., 101*, 20,053–20,082, 1996.

Inoue, H., Y. Fukao, K. Tanabe, and Y. Ogata, Whole mantle *P*-wave travel time tomography, *Phys. Earth Planet. Inter., 59*, 294–328, 1990.

Isaak, D.G., O.L. Anderson, and R.E. Cohen, The relationship between shear and compressional velocities at high pressures: reconciliation of seismic tomography and mineral physics, *Geophys. Res. Lett., 19*, 741–744, 1992.

Ishii, M., and J. Tromp, Normal mode and free-air gravity constraints on lateral variations in velocity and density of Earth's mantle, *Science, 285*, 1231–1236, 1999.

Kanamori, H., and D.L. Anderson, Importance of physical dispersion in surface wave and free oscillations problems: review, *Rev. Geophys. Space Phys., 15*, 105–112, 1977.

Karato, S., Importance of anelasticity in the interpretation of seismic tomography, *Geophys. Res. Lett, 20*, 1623–1626, 1993.

Karato, S., B. Karki, and R. Wentzcovitch, Origin of seismic velocity heterogeneity in the mantle, *EOS Trans AGU, 80*, F939, 1999.

Kennett, B.L.N., and E.R. Engdahl, Traveltimes for global earthquake location and phase identification, *Geophys. J. Int., 105*, 429–465, 1991.

Kennett, B.L.N., E.R. Engdahl, and R. Buland, Constraints on seismic velocities in the Earth from travel times, *Geophys. J. Int, 122*, 108–124, 1995.

Kennett, B.L.N., S. Widiyantoro, and R.D. van der Hilst, Joint seismic tomography for bulk sound and shear wave speed in the Earth's mantle, *J. Geophys. Res., 103*, 12,469–12,493, 1998.

Laske, G., and G. Masters, Constraints on global phase velocity maps by long-period polarization data, *J. Geophys. Res., 101*, 16,059–16,075, 1996.

Lay, T., Q. Williams, and E.J. Garnero, The core–mantle boundary layer and deep Earth dynamics, *Nature, 392*, 461–468, 1998.

Li, X.-D., D. Giardini, and J.H. Woodhouse, The relative amplitudes of mantle heterogeneity in *P*-velocity, *S*-velocity and density from free-oscillation data, *Geophys. J. Int., 105*, 649–657, 1991.

Li, X.-D., and B. Romanowicz, Comparison of global inversions with and without considering cross-branch modal coupling, *Geophys. J. Int., 121*, 695–709, 1995.

Li, X-D., and B. Romanowicz, Global mantle shear-velocity model developed using nonlinear asymptotic coupling theory, *J. Geophys. Res., 101*, 22,245–22,272, 1996.

Masters, G., S. Johnson, G. Laske, and H. Bolton, A shear velocity model of the mantle, *Phil. Trans. R. Soc. Lond., 354A*, 1385–1411, 1996.

Masters, G., T.H. Jordan, P.G. Silver, and F. Gilbert, Aspherical earth structure from fundamental spheroidal-mode data, *Nature, 298*, 609–613, 1982.

Masters, G., G. Laske, and F. Gilbert, Autoregressive estimation of the splitting matrix of free-oscillation multiplets, *Geophys. J. Int.*, in press, 1999.

Montagner, J-P., and T. Tanimoto, Global anisotropy in the upper mantle inferred from the regionalization of phase velocities, *J. Geophys. Res., 95*, 4797–4819, 1990.

Mooney, W.D., G. Laske, and G. Masters, CRUST 5.1: A global crustal model at 5° X 5°, *J. Geophys. Res., 103*, 727–747, 1998.

Morelli, A., A.M. Dziewonski, and J.H. Woodhouse, Anisotropy of the inner core inferred from *PKIKP* travel times, *Geophys. Res. Lett., 13*, 1545–1548, 1986.

Morelli, A., and A.M. Dziewonski, Topography of the core-mantle boundary and lateral homogeneity of the liquid core, *Nature, 325*, 678–683, 1987.

Morelli, A., and A.M. Dziewonski, Body wave traveltimes and a spherically symmetric *P*– and *S*-wave velocity model, *Geophys. J. Int., 112*, 178–194, 1993.

Nolet, G., Seismic wave propagation and seismic tomography, in *In: Nolet, G. (Editor), Seismic Tomography, D. Reidel Publishing Company, Dordrecht*, pp.1–23, 1987.

Pulliam, R.J., *Imaging Earth's interior: Tomographic inversions for mantle P-wave velocity structure*, Ph.D Thesis, U.C. Berkeley, 1991.

Pulliam, R.J., D.W. Vasco, and L.R. Johnson, Tomographic inversions for mantle *P* wave velocity structure based on the minimization of l^2 and l^1 norms of International Seismological Centre travel time residuals, *J. Geophys. Res., 98*, 699–734, 1993.

Resovsky, J.S., and M.H. Ritzwoller, New and refined constraints on three-dimensional Earth structure from normal modes below 3mHz, *J. Geophys. Res, 103*, 783–810, 1998.

Resovsky, J.S., and M.H. Ritzwoller, Regularization uncertainty in density models estimated from normal mode data, *Geophys. Res. Lett., 26*, 2319–2322, 1999.

Ritzwoller, M., G. Masters, and F. Gilbert, Observations of anomalous splitting and their interpretation in terms of aspherical structure, *J. Geophys. Res., 91*, 10,203–10,228, 1986.

Ritzwoller, M., G. Masters, and F. Gilbert, Constraining aspherical structure with low frequency interaction coefficients: Application to uncoupled multiplets, *J. Geophys. Res., 93*, 6369–6396, 1988.

Robertson, G.S., and J.H. Woodhouse, Evidence for proportionality

of P and S heterogeneity in the lower mantle, *Geophys. J. Int.*, *123*, 85–116, 1995.

Robertson, G.S., and J.H. Woodhouse, Ratio of relative S to P velocity heterogeneity in the lower mantle, *J. Geophys. Res.*, *101*, 20,041–20,052, 1996.

Shearer, P.M., K.M. Toy, and J.A. Orcutt, Axi-symmetric earth models and inner core anisotropy, *Nature*, *333*, 228–232, 1988.

Smith, M.F., and G. Masters, Aspherical structure constraints from free oscillation frequency and attenuation measurements, *J. Geophys. Res.*, *94*, 1953–1976, 1989.

Souriau, A., and J.H. Woodhouse, A worldwide comparison of predicted S-wave delays from a three-dimensional upper mantle model with P-wave station corrections, *Phys. Earth Planet. Inter.*, *39*, 75–88, 1985.

Su, W-J., and A.M. Dziewonski, Predominance of long-wavelength heterogeneity in the mantle, *Nature*, *352*, 121–126, 1991.

Su, W-J., R.L. Woodward, and A.M. Dziewonski, Degree 12 model of shear velocity heterogeneity in the mantle, *J. Geophys. Res.*, *99*, 6945–6980, 1994.

Su, W.-J., and A.M. Dziewonski, Simultaneous inversion for 3D variations in shear and bulk velocity in the mantle, *Phys. Earth Planet. Int.*, *100*, 135–156, 1997.

Tanimoto, T., Long-wavelength S-velocity structure throughout the mantle, *Geophys. J. Int.*, *100*, 327–336, 1990.

Toy, K.M., *Tomographic analysis of ISC travel time data for Earth structure*, Ph.D Thesis, Univ. Cal. San Diego, 1989.

Trampert, J., and J.H. Woodhouse, Global phase velocity maps of Love and Rayleigh waves between 40 and 150 seconds, *Geophys. J. Int.*, *122*, 675–690, 1995.

Trampert, J., and J.H. Woodhouse, High-resolution global phase velocity distribution, *Geophys. Res. Let.*, *23*, 21–24, 1996.

van der Hilst, R.D., S. Widiyantoro, and E.R. Engdahl, Evidence for deep mantle circulation from global tomography, *Nature*, *386*, 578–584, 1997.

van der Hilst, R.D., and K. Karason, Compositional Heterogeneity in the Bottom 100 Kilometers of Earth's Mantle: Toward a Hybrid Convection Model, *Science*, *283*, 1885-1889, 1999.

Vasco, D.W., L.R. Johnson, and J. Pulliam, Lateral variations in mantle velocity structure and discontinuities determined from P, PP, S, SS, and $SS - S_dS$ travel times residuals, *J. Geophys. Res.*, *100*, 24,037–24,059, 1995.

Vasco, D.W., and L.R. Johnson, Whole Earth structure estimated from seismic arrival times, *J. Geophys. Res.*, *103*, 2633–2671, 1998.

Vasco, D.W., R.J. Pulliam, and L.R. Johnson, Formal inversion of ISC arrival times for mantle P-velocity structure, *Geophys. J. Int.*, *113*, 586–606, 1993.

Vasco, D.W., R.J. Pulliam, L.R. Johnson, and P.S. Earle, Robust inversion of IASP91 travel time residuals for mantle P and S velocity structure, earthquake mislocations, and station corrections, *J. Geophys. Res.*, *99*, 13,727–13,755, 1994.

Woodhouse, J.H., and A.M. Dziewonski, Mapping of the upper mantle: three-dimensional modeling of earth structure by inversion of seismic waveforms, *J. Geophys. Res.*, *89*, 5953–5986, 1984.

Woodward, R.L., and G. Masters, Global upper mantle structure from long-period differential travel times, *J. Geophys. Res.*, *96*, 6351–6377, 1991a.

Woodward, R.L., and G. Masters, Lower mantle structure from $ScS - S$ differential travel times, *Nature*, *352*, 231–233, 1991b.

Woodward, R.L., and G. Masters, Upper mantle structure from long-period differential travel times and free-oscillation data, *Geophys. J. Int.*, *109*, 275–293, 1992.

York, D., Least squares fitting of a straight line, *Canadian J. Phys.*, *44*, 1079–1086, 1966.

Zhang, Y., and T. Lay, Global surface wave phase velocity variations, *J. Geophys. Res.*, *101*, 8415–8436, 1996.

Zhou, H.-W., A high resolution P wave model for the top 1200 km of the mantle, *J. Geophys. Res.*, *101*, 27,791–27,810, 1996.

G. Laske, IGPP 0225, U.C. San Diego, La Jolla, CA 92093-0225. (e-mail: glaske@ucsd.edu)

G. Masters, IGPP 0225, U.C. San Diego, La Jolla, CA 92093-0225. (e-mail: gmasters@ucsd.edu)

A. Dziewonski, Dept. of Earth and Planetary Sciences, Harvard University, Cambridge, MA 02138. (e-mail: dziewons@geophysics.harvard.edu)

H. Bolton, Albuquerque Seismological Laboratory, Albuquerque, New Mexico 87115-5000 (e-mail: bolton@asl.cr.usgs.gov)